Electronic Journal of Biotechnology 81 (2026) 100709

Contents lists available at ScienceDirect

Electronic Journal of Biotechnology

journal homepage: www.elsevier.com/locate/ejbt

Research article

Identification and validation of a pyroptosis-relevant model for the prognosis of cutaneous melanoma ☆

YaSu Jiang [a,1], YingYing Chen [b,1], ShengFeng Gao [a], MengTing Wang [a], ZhenHua Gong [a,*], JianFeng Ji [a,*]

[a] Department of Burn and Plastic Surgery, Nantong First People's Hospital, Southeast University Affiliated Nantong First People's Hospital, Nantong City, Jiangsu Province, China
[b] Department of Respiratory, Nantong First People's Hospital, Nantong City, Jiangsu Province, China

GRAPHICAL ABSTRACT

Identification and validation of a pyroptosis-relevant model for the prognosis of cutaneous melanoma

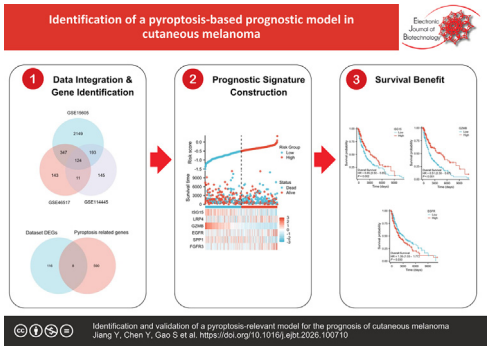

ARTICLE INFO

Article history:
Received 15 September 2025
Accepted 23 January 2026
Available online 17 March 2026

Keywords:
Biomarkers
Gene expression profiling
Immune cell infiltration
Melanoma
Prognosis
Programmed cell death
Pyroptosis
Skin neoplasms
Survival analysis
Tumor microenvironment

ABSTRACT

Background: Cutaneous melanoma (CM) is a highly aggressive skin malignancy with marked molecular heterogeneity and poor prognosis. Pyroptosis, an inflammatory form of programmed cell death, has been implicated in tumor progression and immune regulation; however, its prognostic value in CM remains incompletely understood.

Results: Gene expression data from the Gene Expression Omnibus (GEO) and The Cancer Genome Atlas skin cutaneous melanoma (TCGA-SKCM) cohorts were analyzed to identify pyroptosis-related differentially expressed genes (PRGs). Eight CM-associated PRGs were identified through integrated differential expression and intersection analyses. Functional enrichment analyses revealed that these genes were involved in inflammatory responses, immune regulation, and cell cycle-related pathways. A prognostic model was constructed using univariate Cox and least absolute shrinkage and selection operator (LASSO) regression analyses in the TCGA-SKCM cohort. Six PRGs were incorporated into the prognostic signature, of which ISG15, GZMB, and EGFR were independently associated with patient survival. The model demonstrated good predictive performance, as confirmed by receiver operating characteristic curves, Kaplan-Meier survival analysis, calibration plots, and decision curve analysis at 1-, 3-, and 5-year time points. Immune infiltration analysis revealed that ISG15, GZMB, and EGFR expression were positively correlated with the enrichment of multiple immune cell populations. Mutation profiling

☆ Audio abstract available in Supplementary material.

Peer review under responsibility of Pontificia Universidad Católica de Valparaíso.

* Corresponding authors.
E-mail addresses: gggzhenhua@hotmail.com (Z. Gong), jjfeng1971@outlook.com (J. Ji).

[1] These authors equally contributed to this study.

https://doi.org/10.1016/j.ejbt.2026.100709

further supported the clinical relevance of these prognostic genes.
Conclusions: In summary, we developed a pyroptosis-related prognostic model for cutaneous melanoma and identified ISG15, GZMB, and EGFR as clinically relevant prognostic biomarkers. Our findings enhance the understanding of pyroptosis-associated molecular mechanisms in CM and support their potential utility in prognostic stratification.
How to cite: Jiang Y, Chen Y, Gao S, et al. Identification and validation of a pyroptosis-relevant model for the prognosis of cutaneous melanoma. Electron J Biotechnol 2026;81. https://doi.org/10.1016/j.ejbt.2026.100709.

1. Introduction

Cutaneous melanoma (CM), arising from the malignant transformation of melanocytes, is one of the most aggressive forms of skin cancer [1]. Although CM accounts for approximately 4% of all skin cancer cases, it is responsible for nearly 75% of skin cancer–related deaths [2]. Early-stage melanoma can often be effectively treated by surgical excision, particularly when the primary tumor is thin. However, therapeutic options for metastatic melanoma remain limited. Despite significant advances in targeted therapies and immunotherapies, either alone or in combination, intrinsic and acquired resistance to treatment, as well as treatment-related adverse effects, continue to pose significant clinical challenges [3,4,5,6].

The pronounced biological heterogeneity of melanoma is a key factor underlying therapeutic resistance and variable clinical outcomes [7,8]. With ongoing advances in gene sequencing technologies, attention has increasingly focused on molecular and epigenetic mechanisms in tumor research. Given the complexity of the molecular processes influencing CM progression and prognosis, polygenic models are generally more accurate than single-gene markers for prognostic prediction [9,10,11]. Therefore, identifying reliable prognostic gene signatures is essential for risk stratification, individualized treatment planning, and survival prediction in patients with CM.

Pyroptosis, also known as inflammatory programmed cell death, is characterized by cell swelling, membrane rupture, and the release of intracellular contents, leading to a robust inflammatory response [12]. Accumulating evidence suggests that under chronic inflammatory conditions, pyroptosis-associated signaling may contribute to tumor initiation and progression, while also promoting immune-mediated tumor cell death in certain contexts [13]. Cao et al. previously reported a pyroptosis-related gene signature capable of predicting survival outcomes in patients with skin cutaneous melanoma [14]. However, the relationships among pyroptosis-associated molecular features, temporal dynamics, and clinical outcomes remain incompletely understood. Further investigation into the roles of pyroptosis-related genes (PRGs) and their interactions with the tumor immune microenvironment is therefore warranted. Such studies may improve prognostic assessment and provide insights into novel therapeutic strategies for CM [15].

Several pyroptosis-related prognostic signatures for melanoma have been reported; however, most were derived from a single cohort or platform and may thus reflect cohort-specific effects. In addition, previous models rarely required reproducibility of differentially expressed genes across multiple independent datasets, and immune-microenvironment validation was often limited. To address these gaps, we integrated three independent Gene Expression Omnibus (GEO) cohorts with The Cancer Genome Atlas skin cutaneous melanoma (TCGA-SKCM) cohort and focused on intersecting differentially expressed genes (DEGs) that were consistently dysregulated across platforms. We further constructed two complementary prognostic frameworks, including an immune-linked model, and evaluated clinical utility by decision curve analysis, thereby providing a more generalizable and biologically contextualized pyroptosis-relevant prognosis system for CM. Together, this strategy provides a more generalizable and biologically contextualized prognostic system for pyroptosis in CM.

2. Materials and methods

2.1. Data extraction

Gene expression microarray datasets were obtained from the Gene Expression Omnibus (GEO) database (https://www.ncbi.nlm.nih.gov/geo/), including GSE15605 (58 melanoma, 16 normal), GSE46517 (104 melanoma, 7 normal), and GSE114445 (16 melanoma, 6 normal). These datasets were downloaded using default GEO query settings. Transcriptomic and clinical data for skin cutaneous melanoma were obtained from TCGA-SKCM using the TCGAbiolinks R package with default parameters [16]. We acquired 473 CM samples, each containing comprehensive clinical data. Normalized FPKM expression values and corresponding clinical data were retrieved from the UCSC Xena platform (https://xenabrowser.net/) [17]. The count sequencing data and associated clinical information from the CM dataset (TCGA-SKCM) were normalized using the limma package [18]. PRGs were collected from GeneCards (https://www.genecards.org/) [19] (https://www.genecards.org/) and the Molecular Signatures Database (MSigDB) (https://www.gsea-msigdb.org/) using the keyword "pyroptosis" and default search settings. After removing duplicates, 598 candidate PRGs were retained [20].

2.2. CM-related differentially expressed genes

To identify DEGs associated with CM, the GEO microarray datasets GSE15605, GSE46517, and GSE114445 were normalized and analyzed using the limma package in R with default normalization and linear modeling procedures. Limma was selected because it is specifically designed for microarray-based expression analysis and has been widely validated for differential expression studies [18]. Differential expression analysis was conducted by fitting linear models and applying empirical Bayes moderation. Genes with an absolute log2 fold change ($|\log2FC| > 1$) and an adjusted p-value (Benjamini–Hochberg correction) < 0.05 were defined as significantly differentially expressed. Genes with $\log2FC > 1$ were considered upregulated, whereas genes with $\log2FC < -1$ were considered downregulated. To identify pyroptosis-related DEGs associated with CM, DEGs common to the three GEO datasets were determined using Venn diagram analysis. These overlapping DEGs were further intersected with PRGs to obtain CM-associated pyroptosis-related DEGs. Differential expression results were

visualized using ggplot2 to generate volcano plots and pheatmap to construct heatmaps, both using default visualization parameters.

2.3. Functional enrichment analysis of differentially expressed PRGs

Differentially expressed PRGs were subjected to functional enrichment analysis. Gene Ontology (GO) enrichment analysis, including biological process (BP), cellular component (CC), and molecular function (MF), was performed using the clusterProfiler package in R with default parameters [21,22]. *p*-values were adjusted using the Benjamini–Hochberg method, and terms with adjusted $p < 0.05$ were considered statistically significant. The clusterProfiler package was selected because it is a widely used and well-validated tool for functional enrichment analysis in transcriptomic studies [22].

2.4. GSEA and GSVA

Gene Set Enrichment Analysis (GSEA) was performed to evaluate whether predefined gene sets showed statistically significant differences between biological phenotypes [23]. In this study, phenotypic grouping was defined as tumor versus normal samples within each GEO dataset (GSE15605, GSE46517, and GSE114445), based on their original clinical annotations. Genes were ranked according to their differential expression between the two phenotypes.

GSEA was conducted using the clusterProfiler package with default settings, except where specified. The following parameters were applied: 1000 permutations, minimum gene set size of 10, and maximum gene set size of 500. These gene set size thresholds are recommended to avoid instability caused by excessively small gene sets and dilution effects from overly large gene sets and are consistent with the original GSEA methodology [23]. *p*-values were adjusted using the Benjamini–Hochberg method, and gene sets with adjusted $p < 0.05$ were considered significantly enriched. The c2.cp.v7.2.symbols gene set was obtained from the Molecular Signatures Database (MSigDB) [20].

Gene Set Variation Analysis (GSVA) was performed using the GSVA R package with default kernel estimation and normalization parameters [24]. GSVA is an unsupervised, nonparametric method that estimates pathway activity at the individual-sample level, enabling comparison of pathway enrichment between tumor and normal samples [24]. The h.all.v7.4.symbols.gmt gene set from MSigDB was used to assess pathway activity differences between cutaneous melanoma tissues and normal skin tissues in the GSE15605 dataset.

2.5. Tumor microenvironment analysis

The relative abundance of tumor-infiltrating immune cells was estimated using the single-sample gene set enrichment analysis (ssGSEA) method implemented in R with default parameters. Predefined immune cell gene signatures were used to calculate enrichment scores, which represent the relative infiltration levels of each immune cell type in individual samples [25,26]. The association between pyroptosis-related DEG expression and immune cell infiltration was analyzed in the TCGA-SKCM cohort. Immune infiltration differences between cutaneous melanoma and normal skin samples in the GSE15605 dataset were visualized using the ggplot2 package with default plotting parameters.

2.6. Construction of protein–protein interaction (PPI) networks

Protein–protein interaction (PPI) data for pyroptosis-related differentially expressed genes were obtained from the STRING database (https://string-db.org/). The database was queried using default evidence sources with a minimum interaction confidence score of 0.4 (medium confidence), a commonly used threshold that balances interaction reliability and network coverage [27]. The resulting PPI network was imported into Cytoscape (offline) for visualization and network analysis, using default layout parameters.

2.7. The creation of interaction networks involving mRNA-RBP, mRNA-TF, and mRNA-drug associations

To explore the post-transcriptional and transcriptional regulatory mechanisms of pyroptosis-related differentially expressed genes (DEGs), interaction networks involving mRNA–RNA-binding protein (RBP) and mRNA–transcription factor (TF) associations were constructed. mRNA–RBP interactions were obtained from the starBase database (https://starbase.sysu.edu.cn/), which integrates experimentally validated CLIP-seq and degradome sequencing data [28]. Default query parameters were applied. The miRNA Target Prediction Database (miRDB) was used as a supplementary resource for RBP-related annotation [29].

Transcription factor–gene interactions were identified using the CHIPBase database [30] (version 2.0; https://rna.sysu.edu.cn/chipbase/) and the hTFtarget database [9] (https://bioinfo.life.hust.edu.cn/hTFtarget), both queried with default parameters. These analyses were performed to characterize potential upstream transcriptional regulators of pyroptosis-related DEGs.

In addition, mRNA–drug interaction analysis was conducted solely as an exploratory, hypothesis-generating analysis to determine whether identified prognostic genes have known interactions with existing drugs that could potentially influence gene expression in real-world clinical settings (e.g., patients with comorbidities receiving pharmacological treatment). Importantly, this analysis does not imply therapeutic recommendations and does not affect the diagnostic or prognostic model developed in this study. mRNA–drug interactions were retrieved from the Drug–Gene Interaction Database (DGIdb) (https://www.dgidb.org/) using default query settings [31]. All interaction networks (mRNA–RBP, mRNA–TF, and mRNA–drug) were visualized in Cytoscape using default layout parameters.

2.8. ROC assessment

Receiver operating characteristic (ROC) curve analysis was performed to evaluate the prognostic performance of pyroptosis-related DEGs [32]. ROC curves and corresponding areas under the curve (AUCs) were generated using the survivalROC R package with default parameters. The AUC was used as a measure of discriminative ability, reflecting the balance between sensitivity and specificity. In accordance with commonly accepted clinical interpretation guidelines, AUC values closer to 1.0 indicate stronger discriminative performance, whereas values near 0.5 indicate limited predictive ability [32,33]. These interpretations are widely applied in biomedical and clinical prognostic studies.

2.9. Analysis of clinical associations

Univariate Cox proportional hazards regression analysis was performed to evaluate the association between pyroptosis-related DEGs and patient prognosis in cutaneous melanoma (CM). Variables with *p*-values < 0.1 in univariate analysis were selected for inclusion in multivariate Cox regression models, a commonly used threshold to avoid excluding potentially relevant prognostic factors in multivariable modeling. Cox regression analyses were conducted using the survival R package with default parameters. Based on the results of the multivariate Cox regression

analysis, a prognostic nomogram was constructed to estimate 1-, 3-, and 5-year survival probabilities for CM patients using standard nomogram construction methods.

The predictive performance of the nomogram was evaluated using calibration curves, which compare predicted survival probabilities with observed outcomes. Calibration analysis was performed using default settings. In addition, decision curve analysis (DCA) was conducted to assess the clinical utility of the prognostic model by quantifying net benefit across a range of threshold probabilities. DCA was implemented using the ggDCA R package with default parameters [34]. To further investigate the relationships among gene expression levels, clinicopathological characteristics, and patient outcomes, differential expression analyses of pyroptosis-related prognostic biomarkers were conducted within the TCGA-SKCM cohort. Associations between biomarker expression and clinical variables were evaluated across multiple parameters. Survival outcomes, including overall survival (OS), disease-specific survival (DSS), and progression-free interval (PFI), were analyzed to determine the prognostic relevance of these biomarkers.

2.10. Gene mutation and single-gene analyses

Gene mutation profiles of pyroptosis-related prognostic differentially expressed genes (DEGs) were analyzed using the cBioPortal for Cancer Genomics database (https://www.cbioportal.org/). Mutation data from the TCGA-SKCM cohort were queried and visualized using default filtering and visualization parameters provided by cBioPortal [23]. Protein expression patterns and single-cell expression profiles of pyroptosis-related prognostic biomarkers were examined using the Human Protein Atlas (HPA) database (https://www.proteinatlas.org/) [35]. Tissue-level protein expression and single-cell RNA expression data were retrieved using default query settings. These analyses were performed to further characterize the expression distribution of prognostic genes in human tissues and skin cell populations.

2.11. Statistical analysis

All statistical analyses were performed in R (version 4.1.2) using appropriate packages and default parameter settings, unless otherwise specified. Comparisons between two groups were conducted using the Wilcoxon rank-sum test, while comparisons among more than two groups were performed using the Kruskal–Wallis test. Survival analyses, including overall survival (OS), disease-specific survival (DSS), and progression-free interval (PFI), were conducted using Kaplan–Meier survival curves, and statistical differences between groups were evaluated using the log-rank test. A two-sided p-value < 0.05 was considered statistically significant. A schematic overview of the analysis workflow is presented in Fig. 1.

3. Results

3.1. Gene expression analysis in CM

Gene expression profiles were systematically analyzed to identify DEGs between CM tissues and normal skin tissues across three independent GEO datasets (GSE15605, GSE46517, and GSE114445). Following normalization, differential expression analysis was performed using the limma framework, and genes meeting the criteria of $|\log_2$ fold change (FC)| > 1 and adjusted p-value < 0.05 were considered statistically significant. In the GSE15605 dataset, 18,469 genes were analyzed, of which 2813 were identified as differentially expressed. Among these, 987 genes were upregulated, and 1826 genes were downregulated in melanoma tissues compared with normal skin tissues. The overall distribution and magnitude of differential expression are illustrated in the volcano plot shown in Fig. 2A.

Analysis of the GSE46517 dataset identified 625 DEGs from 12,549 analyzed genes, including 188 upregulated genes and 437 downregulated genes. The corresponding volcano plot is presented in Fig. 2B, demonstrating a distinct separation between differentially expressed and non-differentially expressed genes. Similarly, in the GSE114445 dataset, 473 DEGs were identified among 21,656 analyzed genes, including 270 upregulated and 203 downregulated genes. The results of the differential expression analysis for this dataset are visualized in Fig. 2C. To identify robust CM-associated transcriptional alterations, we next examined the overlap of DEGs across all three GEO datasets. Venn diagram analysis revealed 124 common DEGs shared among GSE15605, GSE46517, and GSE114445 (Fig. 2D), indicating a conserved gene expression signature associated with cutaneous melanoma across independent cohorts. To investigate the involvement of pyroptosis in CM, the shared DEGs were intersected with a curated list of PRGs. This integrative analysis identified eight pyroptosis-related DEGs: MMP1, FGFR3, SPP1, CXCL8, EGFR, GZMB, LRP4, and ISG15 (Fig. 2E). These genes represent potential molecular links between pyroptosis and melanoma pathogenesis.

The expression patterns of these eight pyroptosis-related DEGs were further examined across the three GEO datasets. Heatmap visualization demonstrated consistent and distinct expression differences between melanoma and normal skin samples in GSE15605 (Fig. 2F), GSE46517 (Fig. 2G), and GSE114445 (Fig. 2H). The concordant expression trends observed across independent datasets underscore the robustness of these pyroptosis-associated genes in CM and provide a strong foundation for subsequent functional and prognostic analyses.

3.2. Analysis of functional pathways involving pyroptosis-related DEGs

To characterize the functional roles of pyroptosis-related DEGs in CM, GO enrichment analysis was performed, including BP, CC, and MF categories (Table 1). Enriched GO terms were identified using thresholds of adjusted p < 0.05 and FDR < 0.05. BP enrichment analysis demonstrated that the eight pyroptosis-related DEGs were significantly associated with processes such as ossification, regulation of protein localization to the membrane, response to UV-A radiation, biomineral tissue development, and biomineralization (Fig. 3A). These processes are closely related to skin homeostasis and melanoma biology, particularly UV-induced cellular stress responses and alterations in extracellular matrix remodeling and membrane-associated signaling, which are known contributors to CM initiation and progression.

In the MF category, the enriched terms were predominantly related to transmembrane receptor protein tyrosine kinase activity and transmembrane receptor protein kinase activity (Fig. 3B). These molecular functions are essential for intracellular signal transduction, tumor cell proliferation, and immune-related signaling, suggesting that pyroptosis-related DEGs may influence CM progression through receptor-mediated pathways. Network-based visualization of GO enrichment further illustrated the functional interconnections among enriched BP and MF terms. The BP enrichment network (Fig. 3C) and MF enrichment network (Fig. 3D) revealed coordinated involvement of pyroptosis-related DEGs in membrane-associated signaling, stress-response pathways, and immune-related processes, supporting their potential roles in inflammatory signaling and tumor-microenvironment interactions in CM.

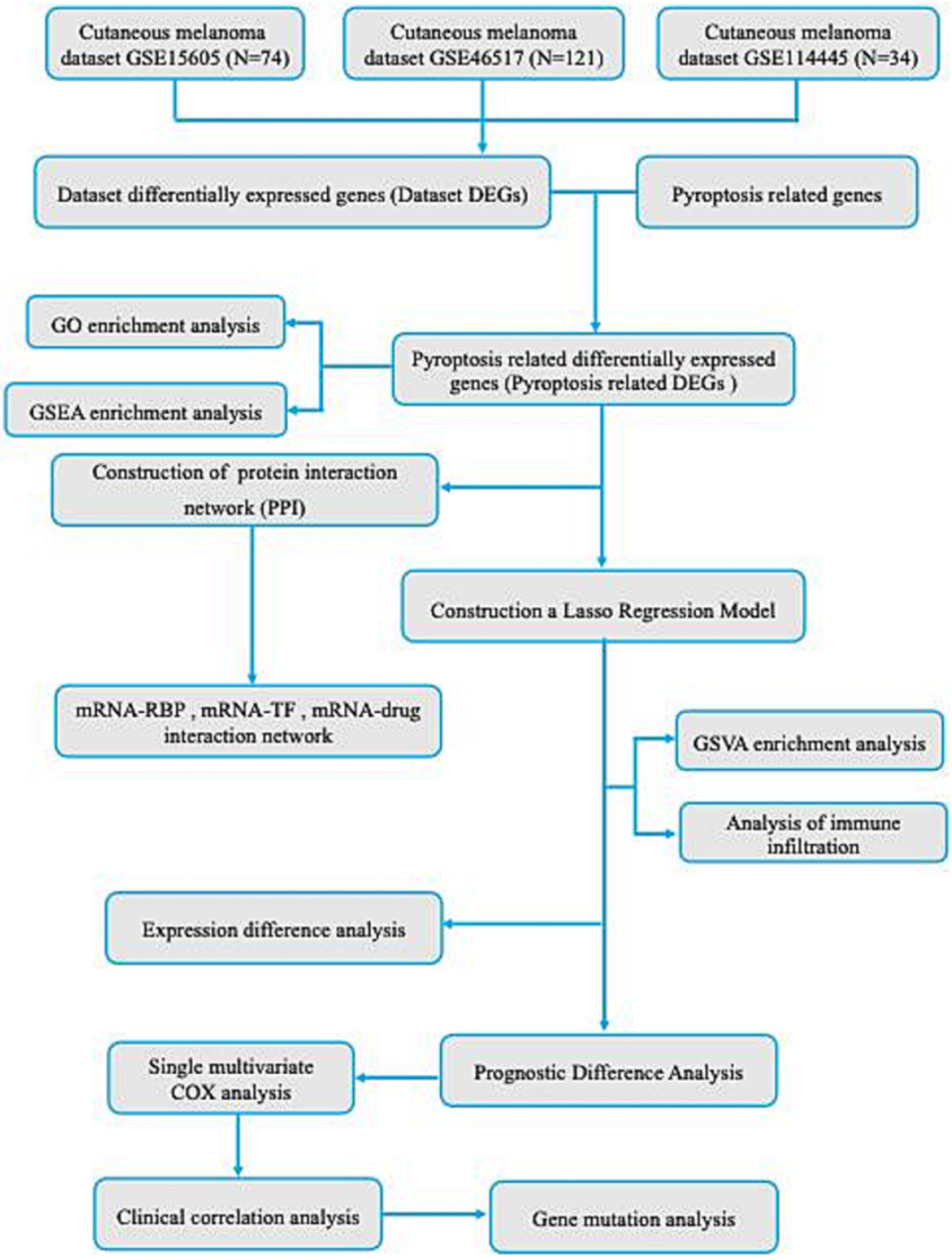

Fig. 1. Workflow. DEGs: differentially expressed genes, GO: Gene Ontology, GSEA: gene set enrichment analysis, PPI network: protein–protein interaction network, RBP: RNA binding protein, TFs: transcription factors, LASSO: least absolute shrinkage and selection operator, GSVA: gene set variation analysis.

3.3. GSEA identifies cell cycle dysregulation and inflammation-associated signaling in CM

GSEA was performed to further investigate pathway-level differences associated with DEG expression patterns in CM across the GSE15605, GSE46517, and GSE114445 datasets. Significantly enriched gene sets were identified using thresholds of $p < 0.05$ and FDR < 0.05. In the GSE15605 dataset, enriched gene sets were primarily associated with epidermal differentiation and cell cycle regulation, including formation of the cornified envelope, keratinization, mitotic spindle checkpoint, separation of sister chromatids, and resolution of sister chromatid cohesion (Fig. 4B–F; Table 2). These pathways reflect dysregulated proliferation and aberrant differentiation processes characteristic of melanoma progression.

Consistent enrichment patterns were observed in the GSE46517 dataset, in which DEGs were significantly associated with M-phase progression, mitotic metaphase and anaphase, formation of the cornified envelope, keratinization, and sister chromatid separation (Fig. 4H–L; Table 3). The recurrence of these pathways across independent datasets highlights conserved alterations in cell cycle control and epidermal structure in CM. Notably, the GSE114445

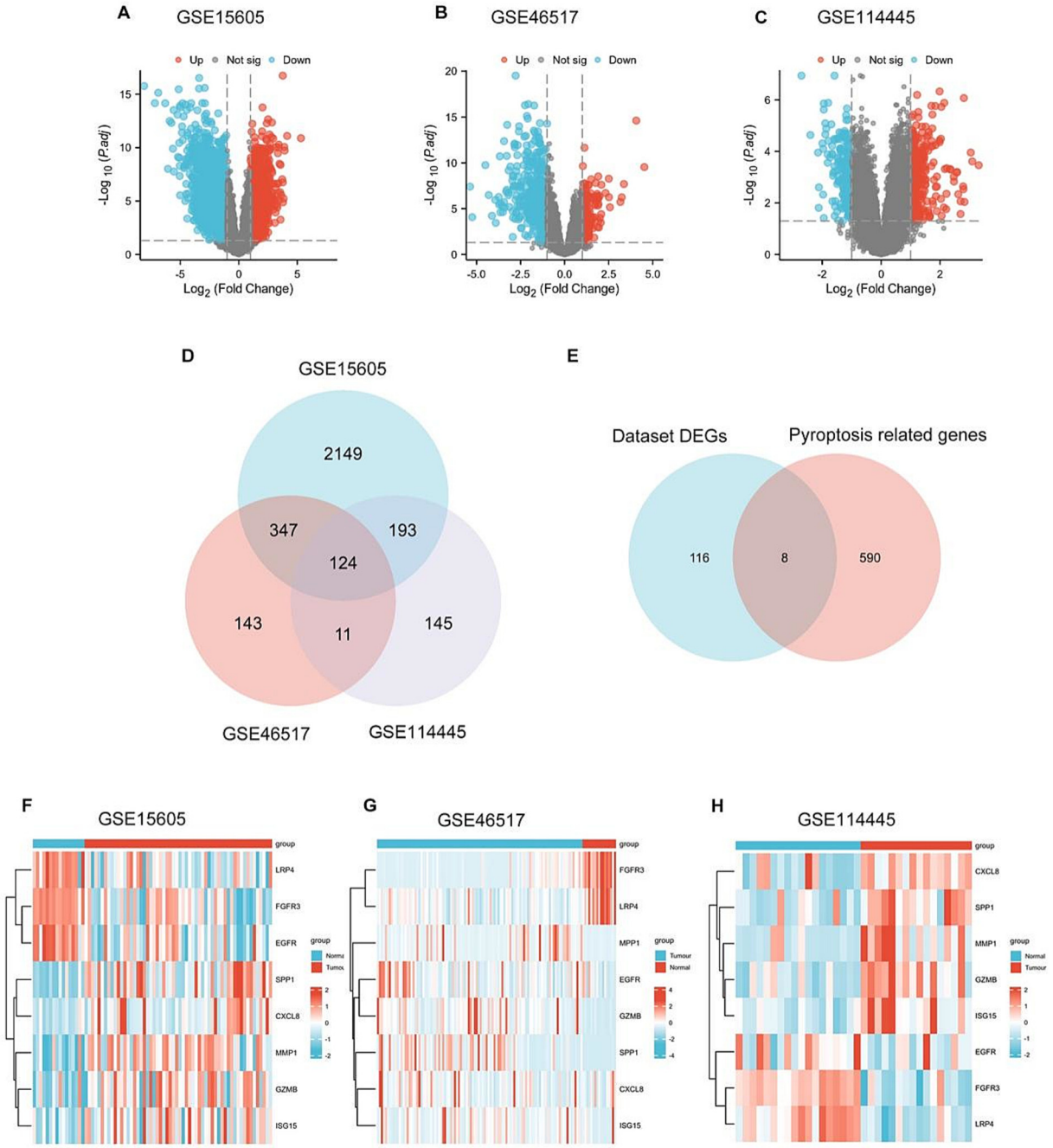

Fig. 2. Analysis of metabolically related differential genes in CM. **A, B, C** Differential gene analysis volcano plot of CM tissues (group: tumor) and adjacent normal tissues (group: normal) of GSE15605 **(A)**, GSE46517 **(B)**, and GSE114445 **(C)** datasets. **(D)** Venn diagram of DEGs in GSE15605, GSE46517, and GSE114445 datasets. **E** Venn diagram of common DEGs (dataset DEGs) and pyroptosis-related genes in the dataset. **F, G, H** Complex numerical heatmaps of pyroptosis-related DEGs in GSE15605 **(F)**, GSE46517 **(G)**, and GSE114445 **(H)** datasets. *CM:* cutaneous melanoma, *DEGs:* differentially expressed genes.

dataset demonstrated enrichment for pathways closely linked to the tumor microenvironment and inflammatory responses, including matrisome-associated pathways, secreted factors, allograft rejection, and signaling for proinflammatory and profibrotic mediators (Fig. 4N–R; Table 4). These results suggest that, in addition to proliferative dysregulation, pyroptosis-related DEGs are involved in extracellular matrix remodeling, immune activation, and inflammation-related processes in CM. Collectively, GSEA across three independent datasets revealed both shared and dataset-specific enrichment patterns, indicating that pyroptosis-related transcriptional alterations in CM are associated with cell cycle dysregulation, epidermal remodeling, and inflammation-related signaling pathways, supporting their biological relevance in melanoma development and progression.

3.4. Establishment of the PPI, mRNA-RBP, mRNA-TF, and mRNA-drug interaction maps

To explore the interaction landscape of pyroptosis-related DEGs in CM, a PPI network was constructed using the STRING database with a confidence threshold of 0.4 and visualized in Cytoscape (Fig. 5A). Among the eight pyroptosis-related DEGs, seven genes (MMP1, FGFR3, SPP1, CXCL8, EGFR, GZMB, and ISG15) formed an interconnected network. Network topology analysis indicated that

Table 1
GO enrichment analysis results of pyroptosis-related differentially expressed genes.

Ontology	ID	Description	Gene ratio	Bg ratio	*p*-value	*p*. adjust	*q* value
BP	GO:0001503	Ossification	5/8	420/18800	2.87948E-07	0	6.85013E-05
BP	GO:1905477	positive regulation of protein localization to membrane	3/8	103/18800	8.76728E-06	0.002	0.001
BP	GO:0070141	response to UV-A	2/8	14/18800	1.43823E-05	0.002	0.001
BP	GO:0031214	biomineral tissue development	3/8	170/18800	3.9348E-05	0.003	0.001
BP	GO:0110148	biomineralization	3/8	172/18800	4.07453E-05	0.003	0.001
BP	GO:1905475	regulation of protein localization to membrane	3/8	172/18800	4.07453E-05	0.003	0.001
BP	GO:0050730	regulation of peptidyl-tyrosine phosphorylation	3/8	261/18800	0	0.01	0.004
BP	GO:0010518	positive regulation of phospholipase activity	2/8	55/18800	0	0.014	0.006
BP	GO:0019058	viral life cycle	3/8	317/18800	0	0.014	0.006
BP	GO:0051205	protein insertion into membrane	2/8	60/18800	0	0.014	0.006
MF	GO:0004714	transmembrane receptor protein tyrosine kinase activity	2/8	60/18410	0	0.011	0.003
MF	GO:0019199	transmembrane receptor protein kinase activity	2/8	79/18410	0	0.011	0.003
MF	GO:0004713	protein tyrosine kinase activity	2/8	135/18410	0.001	0.016	0.005
MF	GO:0019838	growth factor binding	2/8	139/18410	0.001	0.016	0.005
MF	GO:0005178	integrin binding	2/8	156/18410	0.001	0.016	0.005
MF	GO:0004252	serine-type endopeptidase activity	2/8	174/18410	0.002	0.016	0.005
MF	GO:0008236	serine-type peptidase activity	2/8	191/18410	0.002	0.016	0.005
MF	GO:0017171	serine hydrolase activity	2/8	195/18410	0.002	0.016	0.005
MF	GO:0005125	cytokine activity	2/8	235/18410	0.004	0.021	0.006
MF	GO:0031386	protein tag	1/8	13/18410	0.005	0.024	0.007

MMP1 had the highest degree of connectivity, making it the most central hub gene within the PPI network, while EGFR, CXCL8, and SPP1 also displayed multiple interactions, though to a lesser extent. To further characterize post-transcriptional regulation, an mRNA–RBP interaction network was constructed based on starBase data. This network comprised seven mRNAs, 297 RBPs, and 151 mRNA–RBP interaction pairs, highlighting extensive post-transcriptional regulatory potential for pyroptosis-related DEGs (Fig. 5B; Table S1).

Transcriptional regulatory relationships were examined using CHIPBase and hTFtarget databases. Integration of these datasets identified 339 TFs interacting with pyroptosis-related DEGs, and the resulting mRNA–TF network was visualized in Cytoscape (Fig. 5C). Consistent with the PPI analysis, MMP1 demonstrated the highest number of TF interactions, with 37 mRNA–TF interaction pairs, suggesting a prominent role in upstream transcriptional regulation (Table S2).

In addition, mRNA–drug interaction analysis was performed as an exploratory assessment of known drug–gene associations. Using DGIdb, 406 potential drugs or small molecules interacting with seven pyroptosis-related DEGs were identified (Fig. 5D; **Table S3**). Notably, EGFR was associated with the largest number of drug interactions (n = 158), reflecting its well-characterized pharmacological relevance. This analysis was intended to provide contextual information on known gene–drug relationships and does not imply therapeutic application within the scope of the current diagnostic-focused study.

3.5. Development of a prognostic model for differentially expressed genes associated with pyroptosis and GSVA

To construct a robust prognostic model for CM, LASSO regression was applied to the eight pyroptosis-related DEGs in the TCGA-SKCM cohort (Fig. 6A). Unlike conventional regression models, which include all candidate variables and may be affected by multicollinearity and overfitting in high-dimensional transcriptomic data, LASSO regression performs variable selection and coefficient shrinkage simultaneously, enabling the identification of the most informative prognostic features. Based on the optimal penalty parameter, six genes (ISG15, LRP4, GZMB, EGFR, SPP1, and FGFR3) were retained in the LASSO-based prognostic model (Fig. 6B). A risk score was subsequently calculated for each patient using the expression levels of these genes, and patients were stratified into high- and low-risk groups according to the median risk score. The distribution of risk scores, survival status, and expression patterns of the six prognostic DEGs is shown in Fig. 6C, demonstrating clear separation between risk groups.

To further explore the biological characteristics associated with the identified prognostic genes, GSVA was performed to compare pathway activity between CM tumor tissues and normal skin tissues in the GSE15605 dataset. GSVA revealed 50 hallmark gene sets with significant differences between tumor and normal samples (Fig. 6D; Table 5). Among these, pathways related to E2F targets, DNA repair, G2M checkpoint, and mitotic spindle exhibited markedly higher enrichment scores in CM tumor tissues, indicating enhanced proliferative and cell cycle activity. Conversely, pathways including estrogen response late, bile acid metabolism, myogenesis, and cholesterol homeostasis displayed lower enrichment scores in tumor tissues compared with normal skin. These findings suggest that the pyroptosis-related prognostic DEGs identified by LASSO regression are associated with distinct alterations in cell cycle regulation, metabolic processes, and differentiation-related pathways in CM.

3.6. The role of the tumor microenvironment in pyroptosis-related prognostically differentially expressed genes

To investigate the immune landscape associated with pyroptosis-related DEGs in CM, immune cell infiltration was analyzed using ssGSEA. In the GSE15605 dataset, immune infiltration levels were compared between CM tumor tissues and normal skin tissues. The analysis revealed significantly higher infiltration of 10 immune cell types, including CD8 T cells, DCs, iDCs, mast cells, NK CD56bright cells, NK CD56dim cells, Tem cells, Tgd cells, Th1 cells, and Th2 cells, in tumor samples compared with normal controls (Fig. 7A). These results indicate enhanced immune activity within the CM tumor microenvironment.

To further explore the relationship between pyroptosis-related prognostic DEGs and immune infiltration, correlation analyses were performed in the TCGA-SKCM cohort across 24 immune cell types. Notably, the expression of ISG15, GZMB, and EGFR showed significant positive correlations with the enrichment of most immune cell populations (Fig. 7B–D), suggesting that higher expression of these genes is associated with increased immune infiltration and immune activation within the tumor microenvironment. In contrast, the expression levels of LRP4, SPP1, and FGFR3 were significantly negatively correlated with the enrichment of most immune cell types (Fig. 7E–G), suggesting a potential

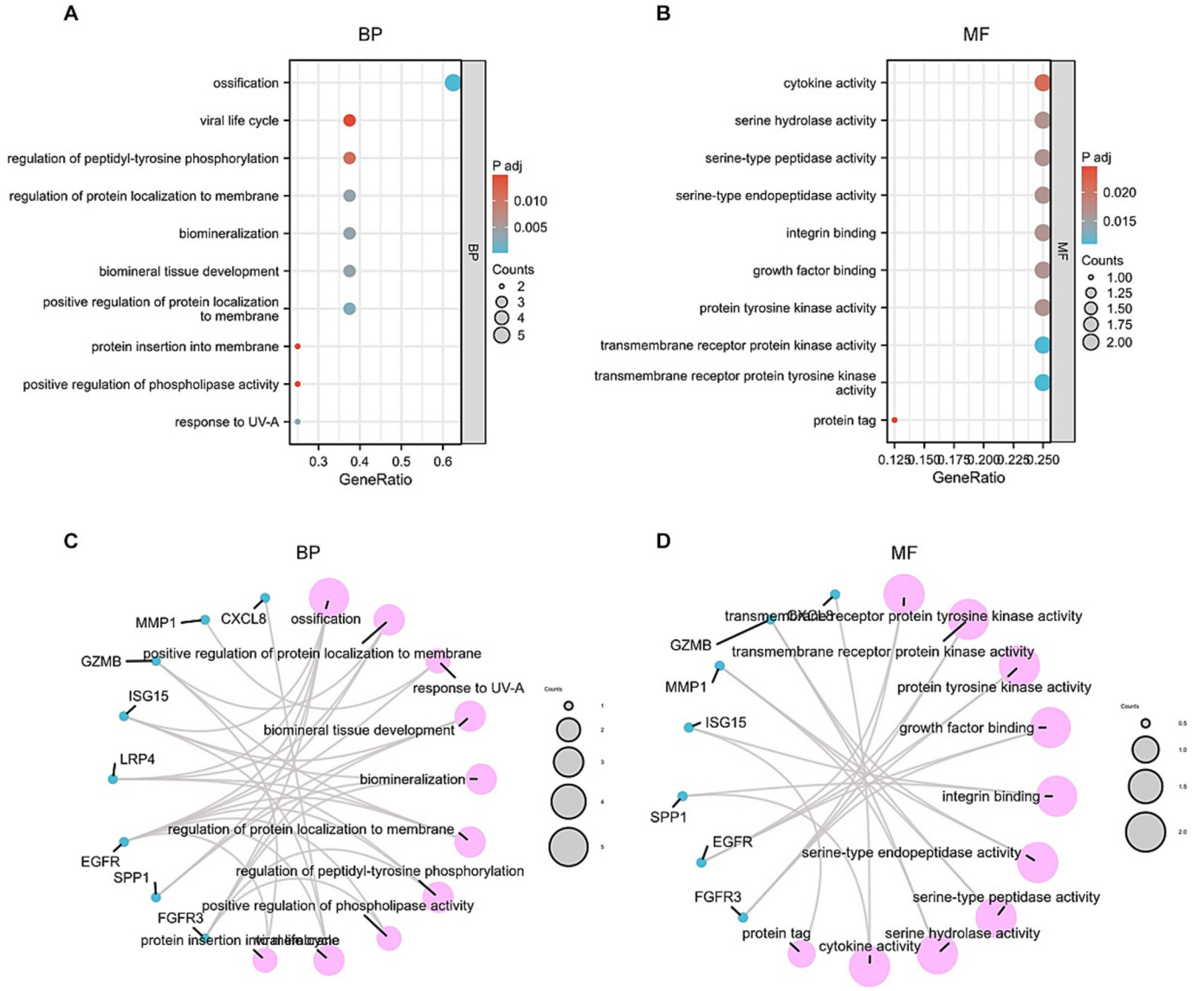

Fig. 3. Functional enrichment analysis (GO) of pyroptosis-related DEGs. **A, B** GO functional enrichment of pyroptosis-related DEGs. BP analysis results in bubble chart display (**A**), MF analysis results in bubble chart display (**B**). **C, D** GO function enrichment of pyroptosis-related DEGs. BP analysis results of ring network diagram display (**C**), MF analysis results of the ring network diagram display (**D**). The bubble color in the bubble plot (**A, B**) indicates the size of the Padj value for GO terms; blue indicates a small Padj value, and red indicates a large Padj value. In the circular network diagram (**C, D**), blue dots represent specific genes, and pink circles represent specific pathways. *p*-value < 0.05 and FDR value (*q* value) < 0.05 were considered to be statistically significant for the functional enrichment analysis entry screening criteria. *GO* Gene Ontology, *BP* biological process, *MF* molecular function. (For interpretation of the references to color in this figure legend, the reader is referred to the web version of this article.)

association with reduced immune infiltration or an immune-suppressive tumor microenvironment. Collectively, these findings demonstrate that pyroptosis-related prognostic DEGs are closely linked to immune cell infiltration patterns in CM.

3.7. Study of prognostic DEGs involved in pyroptosis

The above analyses demonstrated a strong association between the expression of six pyroptosis-related prognostic DEGs and CM. To further evaluate their clinical relevance, expression patterns of these DEGs were examined across TCGA-SKCM and GEO datasets, and their relationships with clinicopathological characteristics were assessed using TCGA-SKCM clinical data (Table 6). ROC curve analysis was performed using the GSE15605 dataset to assess the discriminative performance of the six pyroptosis-related prognostic DEGs (Fig. 8A–F). AUC values were used to assess each gene's ability to distinguish CM tissues from normal skin tissues. In accordance with commonly applied interpretation frameworks in clinical biomarker studies using patient-derived samples, higher AUC values indicate stronger discriminative performance, whereas values closer to 0.5 suggest limited predictive ability.

Among the analyzed genes, ISG15 (AUC = 0.769; Fig. 8A) and GZMB (AUC = 0.779; Fig. 8C) exhibited acceptable discriminative performance, indicating a moderate ability to distinguish CM from normal samples. Notably, FGFR3 (AUC = 0.945; Fig. 8F) demonstrated strong discriminative performance, suggesting high potential clinical relevance. The remaining genes (LRP4, EGFR, and SPP1) also showed meaningful discriminatory capacity, consistent with their selection in the LASSO-based prognostic model. AUC values were interpreted according to established clinical biomarker evaluation criteria: AUC > 0.9 is typically considered excellent discrimination, and values between 0.7 and 0.9 reflect moderate discriminative ability in clinical prognostic studies, such as diagnostic test validations involving patient-derived samples

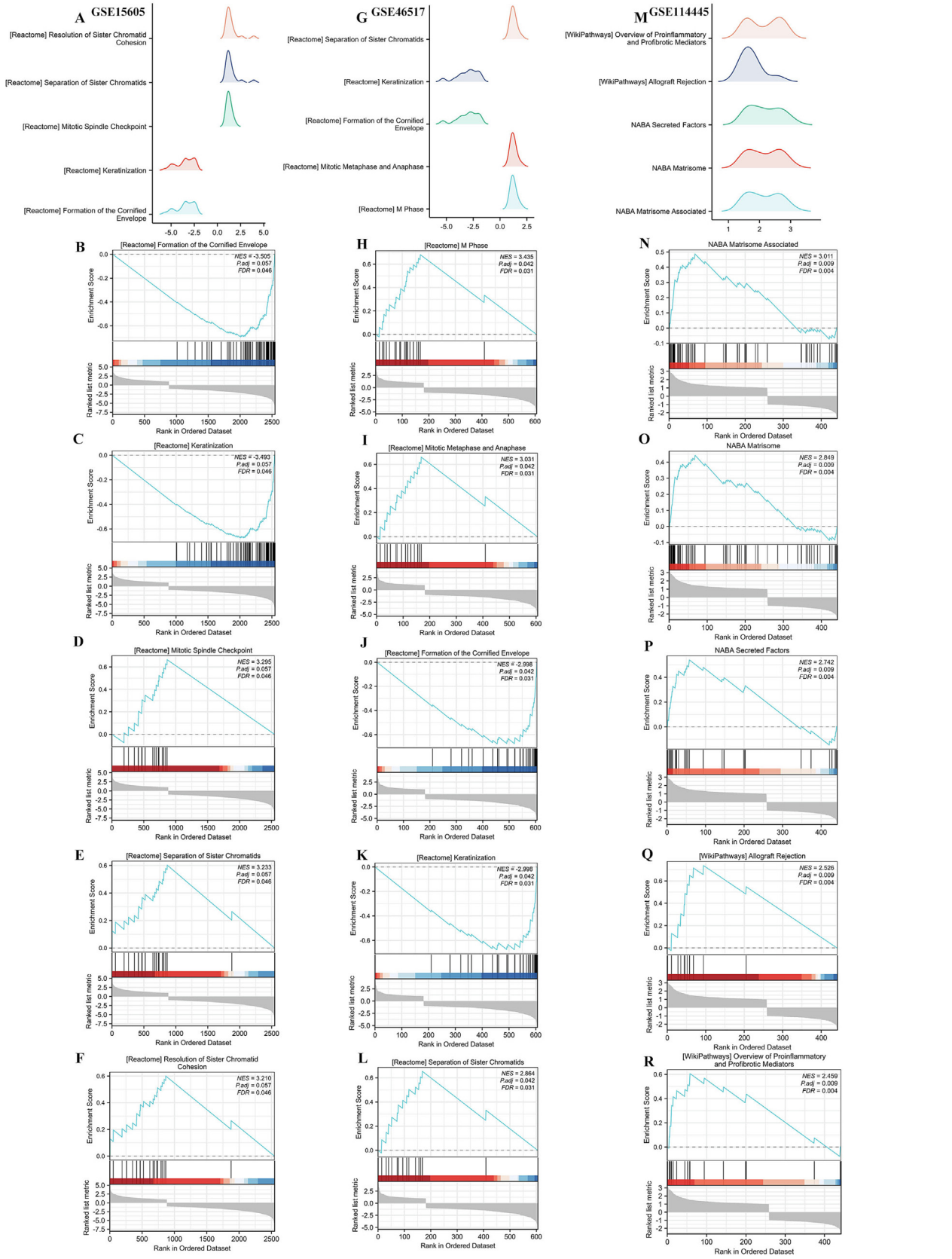

Fig. 4. GSEA enrichment analysis of cutaneous melanoma dataset. **A** GSEA enrichment analysis of the GSE15605 dataset for the main 5 main biological features. **B–F** The DEGs in the GSE15605 dataset were significantly enriched in pathways such as Reactome formation of the cornified envelope (**B**), Reactome keratinization (**C**), Reactome Mitotic spindle checkpoint (**D**), Reactome separation of sister chromatids (**E**), Reactome Resolution of sister chromatid cohesion (**F**). **G** The GSEA analysis of the GSE46517 dataset mainly includes 5 main biological characteristics. **H–L** DEGs in the GSE46517 dataset were significantly enriched in Reactome m phase (**H**), Reactome mitotic metaphase and anaphase (**I**), Reactome formation of the cornified envelope (**J**), Reactome keratinization (**K**), Reactome separation of sister chromatids (**L**). **M** The GSEA analysis of the GSE114445 dataset mainly includes 5 main biological characteristics. **N-R** Reactome matrisome associated (**N**), Reactome matrisome (**O**), Reactome secreted factors (**P**), Reactome allograft rejection (**Q**), Reactome overview of proinflammatory and profibrotic mediators (**R**). The screening criteria for significant enrichment of GSEA analysis results are $p < 0.05$ and FDR value (q value) < 0.05. *DEGs:* differentially expressed genes.

Table 2
GSEA analysis of dataset GSE15605.

Description	Set size	Enrichment score	NES	*p*-value	*p* adjust
REACTOME_FORMATION_OF_THE_CORNIFIED_ENVELOPE	66	−0.693925415	−3.5047563	0.00110742	0.05668621
REACTOME_KERATINIZATION	75	−0.67345626	−3.4932027	0.0010846	0.05668621
REACTOME_MITOTIC_SPINDLE_CHECKPOINT	17	0.664822134	3.29486566	0.00401606	0.05668621
REACTOME_SEPARATION_OF_SISTER_CHROMATIDS	21	0.603005725	3.23299599	0.00444444	0.05668621
REACTOME_RESOLUTION_OF_SISTER_CHROMATID_COHESION	20	0.600643833	3.20959876	0.00421941	0.05668621
REACTOME_RHO_GTPASES_ACTIVATE_FORMINS	20	0.562960785	3.00823573	0.00421941	0.05668621
REACTOME_MITOTIC_METAPHASE_AND_ANAPHASE	23	0.529621127	2.95214176	0.0044843	0.05668621
KEGG_TOLL_LIKE_RECEPTOR_SIGNALING_PATHWAY	14	0.647081762	2.87080085	0.00373134	0.05668621
WP_TOLLLIKE_RECEPTOR_SIGNALING_PATHWAY	14	0.647081762	2.87080085	0.00373134	0.05668621
WP_TYPE_II_INTERFERON_SIGNALING	11	0.715190079	2.80420338	0.00359712	0.05668621
WP_SARSCOV2_INNATE_IMMUNITY_EVASION_AND_CELLSPECIFIC_IMMUNE_RESPONSE	18	0.521541458	2.64300784	0.00423729	0.05668621
WP_TCELL_ACTIVATION_SARSCOV2	12	0.638754537	2.62838783	0.00355872	0.05668621
REACTOME_DNA_REPAIR	11	0.626954419	2.45823838	0.00359712	0.05668621
REACTOME_INTRA_GOLGI_AND_RETROGRADE_GOLGI_TO_ER_TRAFFIC	21	0.455044862	2.43970854	0.00444444	0.05668621
WP_ALLOGRAFT_REJECTION	20	0.451554296	2.41292432	0.00421941	0.05668621

Table 3
GSEA analysis of dataset GSE46517.

Description	Set size	Enrichment score	NES	*p*-value	*p*. adjust
REACTOME_M_PHASE	19	0.681964026	3.43504113	0.00492611	0.04170772
REACTOME_MITOTIC_METAPHASE_AND_ANAPHASE	15	0.660115608	3.03113309	0.00420168	0.04170772
REACTOME_FORMATION_OF_THE_CORNIFIED_ENVELOPE	33	−0.677056563	−2.9978564	0.0011655	0.04170772
REACTOME_KERATINIZATION	33	−0.677056563	−2.9978564	0.0011655	0.04170772
REACTOME_SEPARATION_OF_SISTER_CHROMATIDS	14	0.654011495	2.86369819	0.00420168	0.04170772
REACTOME_MITOTIC_PROMETAPHASE	14	0.653575128	2.86178748	0.00420168	0.04170772
REACTOME_CELL_CYCLE_CHECKPOINTS	15	0.614415774	2.8212876	0.00420168	0.04170772
REACTOME_MITOTIC_SPINDLE_CHECKPOINT	11	0.735690236	2.82030757	0.00373134	0.04170772
REACTOME_DEVELOPMENTAL_BIOLOGY	79	−0.518136659	−2.7444975	0.00107066	0.04170772
REACTOME_APC_C_MEDIATED_DEGRADATION_OF_CELL_CYCLE_PROTEINS	11	0.713804714	2.73640826	0.00373134	0.04170772
REACTOME_RESOLUTION_OF_SISTER_CHROMATID_COHESION	12	0.638470882	2.558798	0.00387597	0.04170772
WP_NETWORK_MAP_OF_SARSCOV2_SIGNALING_PATHWAY	21	0.41198059	2.25129523	0.00492611	0.04170772
WP_OVERVIEW_OF_PROINFLAMMATORY_AND_PROFIBROTIC_MEDIATORS	19	0.439735141	2.21493838	0.00492611	0.04170772
WP_HAIR_FOLLICLE_DEVELOPMENT_CYTODIFFERENTIATION_PART_3_OF_3	23	−0.5463908	−2.168208	0.00243902	0.04170772
REACTOME_NEUTROPHIL_DEGRANULATION	24	−0.468322353	−1.882999	0.00362757	0.04170772

Table 4
GSEA analysis of dataset GSE114445.

Description	Set size	Enrichment score	NES	*p*-value	*p* adjust
NABA_MATRISOME_ASSOCIATED	52	0.487427029	3.01096378	0.00136799	0.00868946
NABA_MATRISOME	60	0.443377593	2.84902163	0.00135135	0.00868946
NABA_SECRETED_FACTORS	29	0.540634309	2.74221111	0.00149254	0.00868946
WP_ALLOGRAFT_REJECTION	10	0.737918659	2.52643622	0.0017094	0.00868946
WP_OVERVIEW_OF_PROINFLAMMATORY_AND_PROFIBROTIC_MEDIATORS	16	0.605733695	2.45911148	0.00161812	0.00868946
KEGG_CHEMOKINE_SIGNALING_PATHWAY	17	0.5649845	2.3568847	0.00159236	0.00868946
WP_NETWORK_MAP_OF_SARSCOV2_SIGNALING_PATHWAY	19	0.524921386	2.27050714	0.00156986	0.00868946
REACTOME_INNATE_IMMUNE_SYSTEM	54	0.360663372	2.25327096	0.00137363	0.00868946
REACTOME_CHEMOKINE_RECEPTORS_BIND_CHEMOKINES	15	0.552488901	2.21517626	0.0015873	0.00868946
KEGG_TOLL_LIKE_RECEPTOR_SIGNALING_PATHWAY	12	0.591669155	2.15786715	0.00167785	0.00868946
WP_TOLLLIKE_RECEPTOR_SIGNALING_PATHWAY	12	0.591669155	2.15786715	0.00167785	0.00868946
REACTOME_ADAPTIVE_IMMUNE_SYSTEM	31	0.406380165	2.13007345	0.00146199	0.00868946
REACTOME_G_ALPHA_I_SIGNALLING_EVENTS	23	0.437007373	2.00583658	0.00316456	0.01484907
WP_LUNG_FIBROSIS	11	0.607984917	2.16887938	0.00504202	0.01646424
WP_HAIR_FOLLICLE_DEVELOPMENT_CYTODIFFERENTIATION_PART_3_OF_3	11	−0.539178939	−2.0828892	0.004914	0.01646424

[23,32,36]. Overall, these findings indicate that pyroptosis-related prognostic DEGs exhibit varying but biologically relevant discriminative performance in CM. Importantly, ROC results were interpreted in conjunction with survival and multivariate analyses, supporting the robustness of the identified prognostic gene signature rather than relying solely on single-gene diagnostic performance.

3.8. Investigation into the prognostic performance and significance of pyroptosis-related DEGs

The prognostic performance of pyroptosis-related DEGs was evaluated using the LASSO-based risk model constructed from six genes (ISG15, LRP4, GZMB, EGFR, SPP1, and FGFR3). Based on the calculated risk scores, patients in the TCGA-SKCM cohort were stratified into high- and low-risk groups. Kaplan–Meier analysis demonstrated a significant difference in overall survival between the two groups, indicating that the LASSO-derived model effectively discriminated patient prognosis ($p < 0.001$; Fig. 9A).

To further assess the prognostic relevance of individual genes, Kaplan–Meier survival analyses were performed for each of the six pyroptosis-related DEGs. Among them, ISG15 ($p = 0.002$; Fig. 9B), GZMB ($p < 0.001$; Fig. 9D), and EGFR ($p = 0.030$; Fig. 9E) were significantly associated with patient survival. In contrast, LRP4 ($p = 0.060$; Fig. 9C), SPP1 ($p = 0.092$; Fig. 9F), and FGFR3 ($p = 0.383$; Fig. 9G) did not show statistically significant associa-

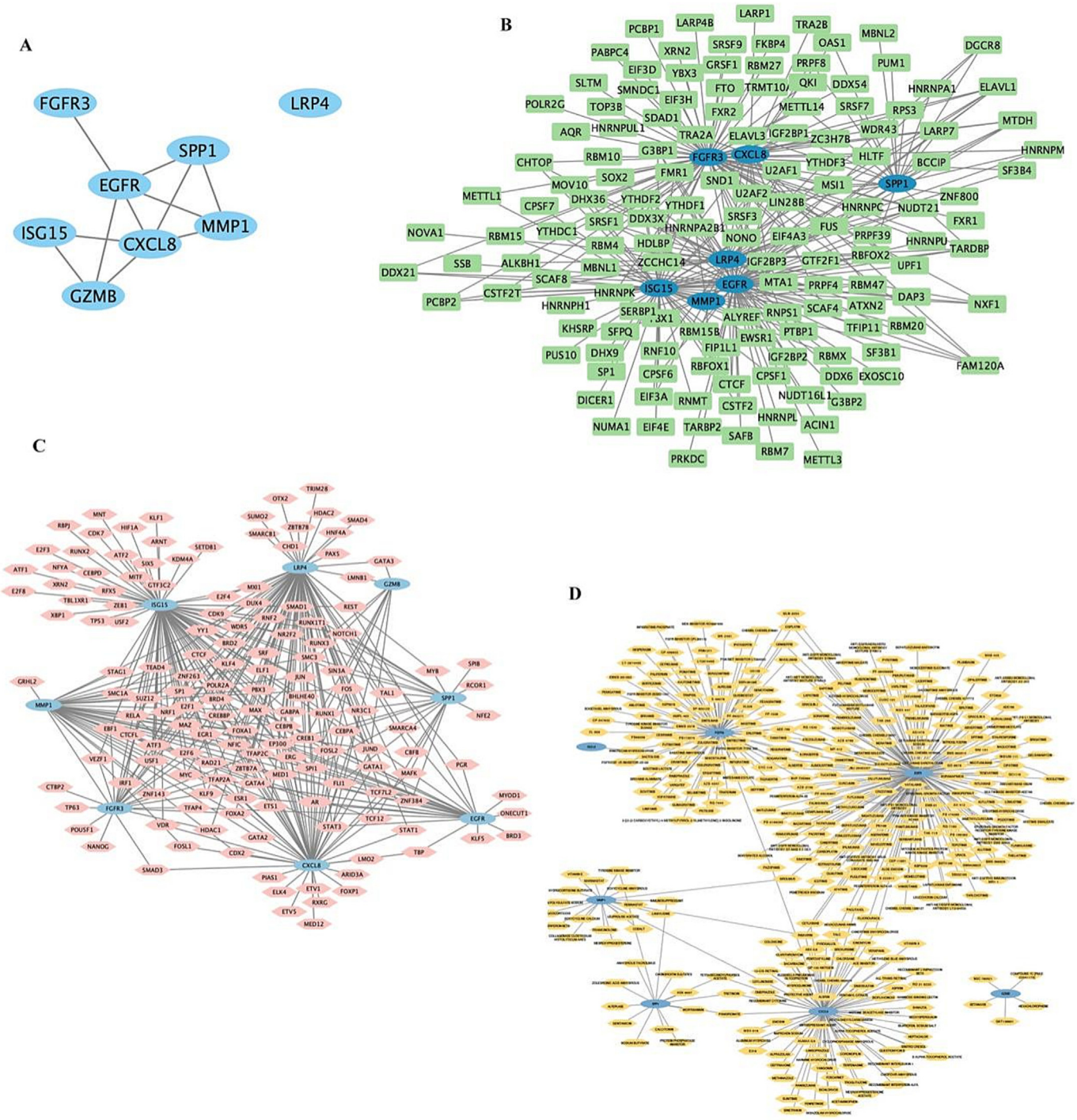

Fig. 5. Construction of protein–protein interaction network (PPI), mRNA-RBP and mRNA-TF. **A** Protein interaction network (PPI) of DEGs related to pyroptosis. **B, C** The mRNA-RBP (**B**) and mRNA-TF (**C**) interaction networks of DEGs related to pyroptosis. In the mRNA-RBP (**B**) interaction network, the dark blue oval block is mRNA; the green block is RBP. In the mRNA-TF (**C**) interaction network, the dark blue oval block is mRNA; the pink diamond block is TF. In the mRNA-drugs **(D)** interaction network, the blue oval block is mRNA; the orange hexagonal block is the drug. *TF* transcription factor; *RBP* RNA binding protein. (For interpretation of the references to color in this figure legend, the reader is referred to the web version of this article.)

tions with survival in the TCGA-SKCM cohort. To validate whether the identified genes were independent prognostic factors, univariate and multivariate Cox regression analyses were conducted. The results demonstrated that ISG15, GZMB, and EGFR remained significantly associated with patient prognosis after adjustment for clinical variables, including T stage, N stage, and age (Table 7). The hazard ratios and confidence intervals derived from Cox regression analyses are summarized in the forest plot shown in Fig. 10A.

Based on the multivariate Cox regression results, a prognostic nomogram was constructed to estimate 1-, 3-, and 5-year survival probabilities for CM patients (Fig. 10B). Calibration analysis demonstrated good agreement between predicted and observed survival outcomes at all three time points, indicating satisfactory predictive accuracy of the nomogram (Fig. 10C). Finally, DCA was performed to evaluate the clinical utility of the LASSO-Cox regression model. The DCA curves for 1-year, 3-year, and 5-year survival

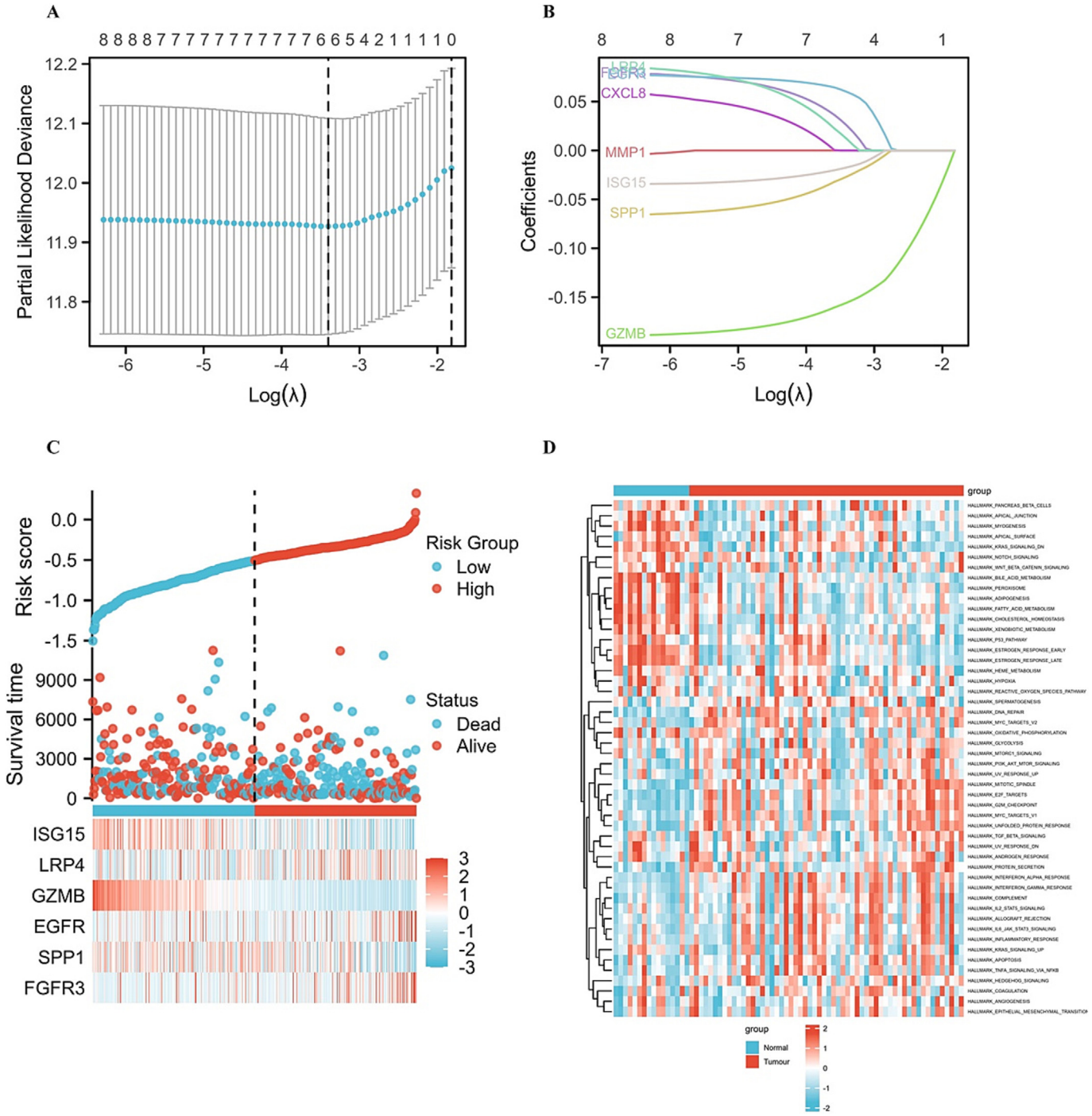

Fig. 6. Construction of a prognostic model of pyroptosis-related DEGs and GSVA analysis. **A** LASSO regression prognostic model diagram of pyroptosis-related DEGs. **B, C** LASSO regression prognostic model variable trajectory plot (**B**), risk factor plot (**C**). **D** GSVA analysis results of pyroptosis-related prognostic DEGs. The screening standard of significant enrichment of GSEA analysis results is $p < 0.05$. *GSVA* gene set variation analysis, *LASSO* least absolute shrinkage and selection operator.

consistently showed that the prognostic model provided a higher net benefit across a wide range of threshold probabilities than default strategies (Fig. 10D–F), supporting its potential clinical applicability for prognostic assessment of CM.

3.9. Clinical examination of prognostic DEGs involved in pyroptosis

To further investigate the clinical relevance of pyroptosis-related prognostic DEGs in CM, associations between gene expression and patient survival outcomes were evaluated using TCGA-SKCM clinical data. From the eight CM-PRGs, six genes (ISG15, LRP4, GZMB, EGFR, SPP1, and FGFR3) were initially selected through LASSO-Cox regression to construct the prognostic signature. Subsequent Kaplan–Meier survival analysis and multivariate Cox regression confirmed that ISG15, GZMB, and EGFR retained independent prognostic significance. These three genes were therefore incorporated into the final immune-associated prognostic framework for CM. The prognostic impact of ISG15, GZMB, and EGFR expression was further examined with respect to OS, DSS, and PFI (Fig. 11A–I). Elevated expression of ISG15 was

Table 5
GSVA analysis of dataset GSE15605.

ID	logFC	AveExpr	t	P-value	adj. P. Val	B
HALLMARK_ESTROGEN_RESPONSE_LATE	−0.3552306	0.00523445	−6.1049274	3.21E-08	9.80E-07	8.53916706
HALLMARK_E2F_TARGETS	0.46249879	0.00036802	6.0585138	3.92E-08	9.80E-07	8.34538334
HALLMARK_BILE_ACID_METABOLISM	−0.336187	−0.006659	−5.7706973	1.34E-07	2.23E-06	7.15656237
HALLMARK_MYOGENESIS	−0.2773486	−0.0105327	−5.5989902	2.75E-07	3.44E-06	6.4587392
HALLMARK_CHOLESTEROL_HOMEOSTASIS	−0.3057454	−0.0082706	−5.4886436	4.36E-07	4.36E-06	6.01518322
HALLMARK_DNA_REPAIR	0.30979784	0.00722165	5.32013451	8.72E-07	6.46E-06	5.34571371
HALLMARK_G2M_CHECKPOINT	0.39741293	0.00401032	5.31105594	9.05E-07	6.46E-06	5.30992671
HALLMARK_ESTROGEN_RESPONSE_EARLY	−0.3020971	0.00459429	−5.2300574	1.26E-06	7.86E-06	4.99195463
HALLMARK_KRAS_SIGNALING_DN	−0.249785	0.00500806	−4.9908124	3.29E-06	1.83E-05	4.06720896
HALLMARK_MITOTIC_SPINDLE	0.25547671	0.0086382	4.93870244	4.05E-06	2.02E-05	3.86879192
HALLMARK_FATTY_ACID_METABOLISM	−0.2619928	−0.0103595	−4.5547091	1.79E-05	8.05E-05	2.44262306
HALLMARK_UNFOLDED_PROTEIN_RESPONSE	0.31016723	0.00412745	4.5352222	1.93E-05	8.05E-05	2.37202756
HALLMARK_INTERFERON_ALPHA_RESPONSE	0.4442234	−0.0105498	4.47649369	2.41E-05	9.27E-05	2.1603652
HALLMARK_ADIPOGENESIS	−0.2665832	−0.0123876	−4.453262	2.63E-05	9.40E-05	2.07709516
HALLMARK_PROTEIN_SECRETION	0.27135108	0.00822356	4.24564564	5.68E-05	0.00018929	1.3448452
HALLMARK_XENOBIOTIC_METABOLISM	−0.2123322	0.00238003	−4.2052057	6.58E-05	0.00020567	1.2047824
HALLMARK_PEROXISOME	−0.1907361	−0.0058166	−3.8994136	0.00019559	0.00057527	0.17432922
HALLMARK_PI3K_AKT_MTOR_SIGNALING	0.19014358	0.0120888	3.6807231	0.00041366	0.00114907	−0.5298252
HALLMARK_COMPLEMENT	0.22382884	0.00736163	3.49630237	0.00076211	0.00200554	−1.1009616
HALLMARK_INTERFERON_GAMMA_RESPONSE	0.32337868	−0.0049694	3.4413436	0.00091086	0.00227716	−1.2669894
HALLMARK_MYC_TARGETS_V1	0.29057711	0.00618932	3.41976926	0.00097643	0.00232484	−1.3316288
HALLMARK_MYC_TARGETS_V2	0.23894629	0.00150777	2.86773196	0.00524628	0.01192337	−2.8775759
HALLMARK_NOTCH_SIGNALING	−0.1449621	−0.01517	−2.7612072	0.00709531	0.01542459	−3.1507063
HALLMARK_ALLOGRAFT_REJECTION	0.24294467	0.00040595	2.66636081	0.00922422	0.01874484	−3.3866662
HALLMARK_APOPTOSIS	0.13210961	0.01128387	2.66052731	0.00937242	0.01874484	−3.4009536
HALLMARK_TNFA_SIGNALING_VIA_NFKB	0.19163996	0.00124812	2.61086909	0.01072429	0.02062363	−3.5215087
HALLMARK_APICAL_JUNCTION	−0.1160385	0.00194128	−2.509388	0.01404926	0.02601715	−3.7618743
HALLMARK_PANCREAS_BETA_CELLS	−0.1257018	0.00386981	−2.42739	0.01738363	0.0310422	−3.9501226
HALLMARK_UV_RESPONSE_UP	0.11519184	0.00569211	2.29791665	0.02409715	0.04154681	−4.2362938
HALLMARK_IL2_STAT5_SIGNALING	0.10114653	0.00732942	1.80486785	0.0747425	0.12060009	−5.1970853
HALLMARK_IL6_JAK_STAT3_SIGNALING	0.13570259	−0.0017138	1.80468074	0.07477206	0.12060009	−5.1974099
HALLMARK_P53_PATHWAY	−0.0742735	0.00480348	−1.5389604	0.12763925	0.1986674	−5.626681
HALLMARK_HEME_METABOLISM	−0.0592492	0.00184285	−1.5248458	0.13112048	0.1986674	−5.6476907
HALLMARK_WNT_BETA_CATENIN_SIGNALING	−0.0823701	−0.0090859	−1.4968067	0.13825812	0.20332076	−5.6888844
HALLMARK_INFLAMMATORY_RESPONSE	0.11235321	0.00030054	1.45997576	0.1480928	0.20614158	−5.7418943
HALLMARK_COAGULATION	0.0694333	0.00896561	1.45877657	0.14842194	0.20614158	−5.7435992
HALLMARK_APICAL_SURFACE	−0.0776044	0.00666986	−1.4391951	0.15387714	0.20794208	−5.7712502
HALLMARK_MTORC1_SIGNALING	0.09245359	0.0067485	1.38937277	0.16845643	0.22098998	−5.840001
HALLMARK_TGF_BETA_SIGNALING	0.08349612	0.00307249	1.3765572	0.17237218	0.22098998	−5.8573121
HALLMARK_OXIDATIVE_PHOSPHORYLATION	−0.1055574	0.00054639	−1.2562596	0.21256619	0.26570773	−6.0123157
HALLMARK_HYPOXIA	−0.0618201	0.00618637	−1.1826637	0.24033824	0.29309541	−6.1004229
HALLMARK_HEDGEHOG_SIGNALING	0.0603932	0.00184103	1.15897012	0.24981063	0.29739361	−6.1276955
HALLMARK_EPITHELIAL_MESENCHYMAL_TRANSITION	0.07908182	−0.0021911	1.10351722	0.27300973	0.31745317	−6.1894346
HALLMARK_SPERMATOGENESIS	0.04240557	−0.0005832	1.00806187	0.31637105	0.35951256	−6.2888185
HALLMARK_GLYCOLYSIS	0.04242968	0.0009774	0.84688057	0.39951068	0.44390076	−6.4366856
HALLMARK_REACTIVE_OXYGEN_SPECIES_PATHWAY	−0.0317087	0.00687532	−0.4815595	0.63139327	0.68629703	−6.6778517
HALLMARK_ANGIOGENESIS	0.03121967	−0.0117536	0.46192418	0.64535099	0.6865436	−6.687086
HALLMARK_ANDROGEN_RESPONSE	−0.0216723	0.00762615	−0.434485	0.66507016	0.69278141	−6.6993499
HALLMARK_KRAS_SIGNALING_UP	−0.014198	0.00611951	−0.2391106	0.81161262	0.82817614	−6.7650296
HALLMARK_UV_RESPONSE_DN	0.00182154	−0.000401	0.03704628	0.97053757	0.97053757	−6.7929106

GSVA gene set variation analysis.

significantly associated with improved OS (p = 0.0005; Fig. 11A), DSS (p = 0.0019; Fig. 11B), and PFI (p = 0.015; Fig. 11C). Similarly, higher expression of GZMB was significantly correlated with favorable OS (p < 0.001; Fig. 11D), DSS (p < 0.001; Fig. 11E), and PFI (p = 0.005; Fig. 11F).

In contrast, EGFR expression demonstrated a distinct prognostic pattern. Higher EGFR expression was significantly associated with OS (p = 0.0114; Fig. 11G) and DSS (p = 0.0257; Fig. 11H), whereas no statistically significant association was observed with PFI (p = 0.0930; Fig. 11I). These results suggest that EGFR may exert differential effects on long-term survival outcomes compared with disease progression dynamics in CM. Collectively, these findings indicate that ISG15 and GZMB are consistently associated with favorable survival outcomes across multiple clinical endpoints, while EGFR exhibits selective prognostic relevance. This highlights the heterogeneous clinical impact of pyroptosis-related DEGs and supports their utility in prognostic stratification of CM patients.

3.10. Mutation profiling of prognostic DEGs linked to pyroptosis

Mutation profiling of the three pyroptosis-related prognostic DEGs (ISG15, GZMB, and EGFR) was performed using the TCGA-SKCM cohort via cBioPortal to characterize their genomic alteration patterns (Fig. 12). Across the cohort, genetic alterations affecting these genes included missense mutations, splice-site mutations, truncating mutations, gene amplification, and deep deletions (Fig. 12A). Among the three genes, EGFR exhibited the highest alteration frequency, with genomic alterations detected

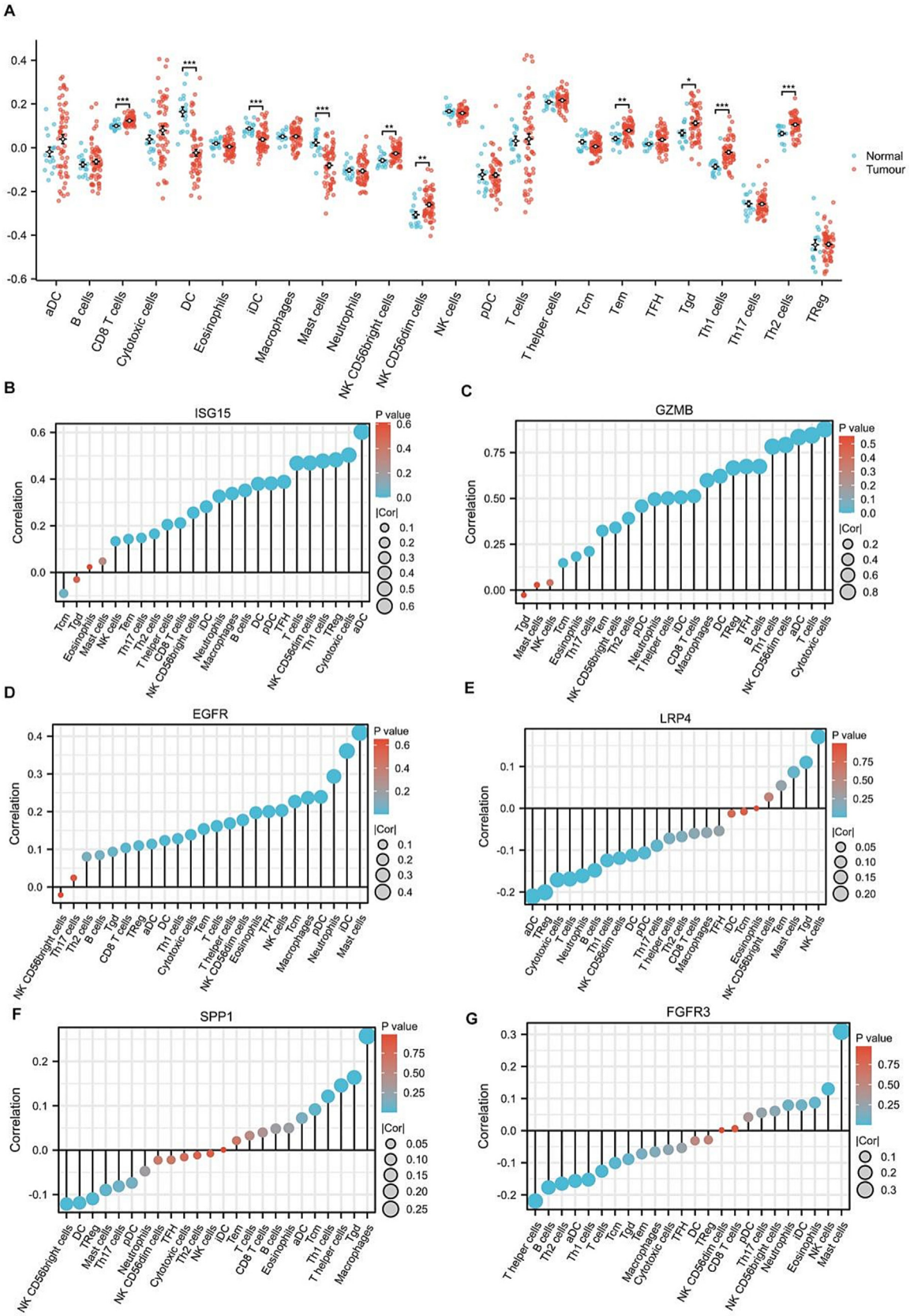

Fig. 7. Assessment of the tumor microenvironment of DEGs associated with pyroptosis. **(A)** The immune infiltration results of the dataset GSE15605 are grouped and compared. **(B–G)** Pyroptosis-related prognostic DEGs *ISG15* (**B**), *GZMB* **(C)**, *EGFR* **(D)**, *LRP4* **(E)**, SPP1 **(F)**, and FGFR3 **(G)** in the TCGA-SKCM data set. The correlation results show that the expression of immune cells. The symbol * is equivalent to $p \leq 0.05$, which is statistically significant; the symbol ** is equivalent to $p \leq 0.01$, which is highly statistically significant; the symbol *** is equivalent to ≤0.001, highly statistically significant. *ssGSEA* single-sample gene-set enrichment analysis, *TCGA* The cancer genome atlas, *SKCM* cutaneous melanoma.

Table 6
Patient characteristics of CM patients in the TCGA datasets.

Characteristic	Levels	Overall
N		351
T stage, *n* (%)	T1	40 (11.3%)
	T2	74 (21%)
	T3	90 (25.6%)
	T4	147 (41.9%)
N stage, *n* (%)	NX	26 (7.4%)
	N0	199 (56.7%)
	N1	59 (16.8%)
	N2	31 (8.8%)
	N3	36 (10.3%)
M stage, *n* (%)	M0	339 (96.6%)
	M1	12 (3.4%)
Pathologic stage, *n* (%)	Stage I	77 (21.9%)
	Stage II	138 (39.3%)
	Stage III	124 (35.3%)
	Stage IV	12 (3.4%)
Age, *n* (%)	≤65	223 (63.5%)
	>65	128 (36.5%)
OS event, n (%)	Alive	178 (50.7%)
	Dead	173 (49.3%)

in approximately 12% of TCGA-SKCM samples. In contrast, GZMB and ISG15 showed relatively lower alteration frequencies (~2.2% and ~1.7%, respectively). Missense mutations and copy-number amplifications dominated EGFR alterations, consistent with its established role as a genomically unstable oncogenic driver in CM. In contrast, alterations in ISG15 and GZMB were primarily composed of missense mutations and copy number changes. Further analysis of mutation distribution revealed that ISG15 mutations were limited in number and predominantly localized to exon 2, with all detected variants classified as uncertain significance (Fig. 12B). GZMB mutations were distributed across exons 2–4, with several missense variants located at phosphorylation-associated sites, suggesting potential effects on immune-related protease activity (Fig. 12C).

Notably, EGFR mutations were widely distributed across exons 1–28 and involved multiple protein domains, including extracellular, transmembrane, and cytoplasmic regions (Fig. 12D). These alterations encompassed missense, splice-site, and truncating mutations, as well as amplification events, reflecting substantial structural and functional diversity. Collectively, mutation profiling

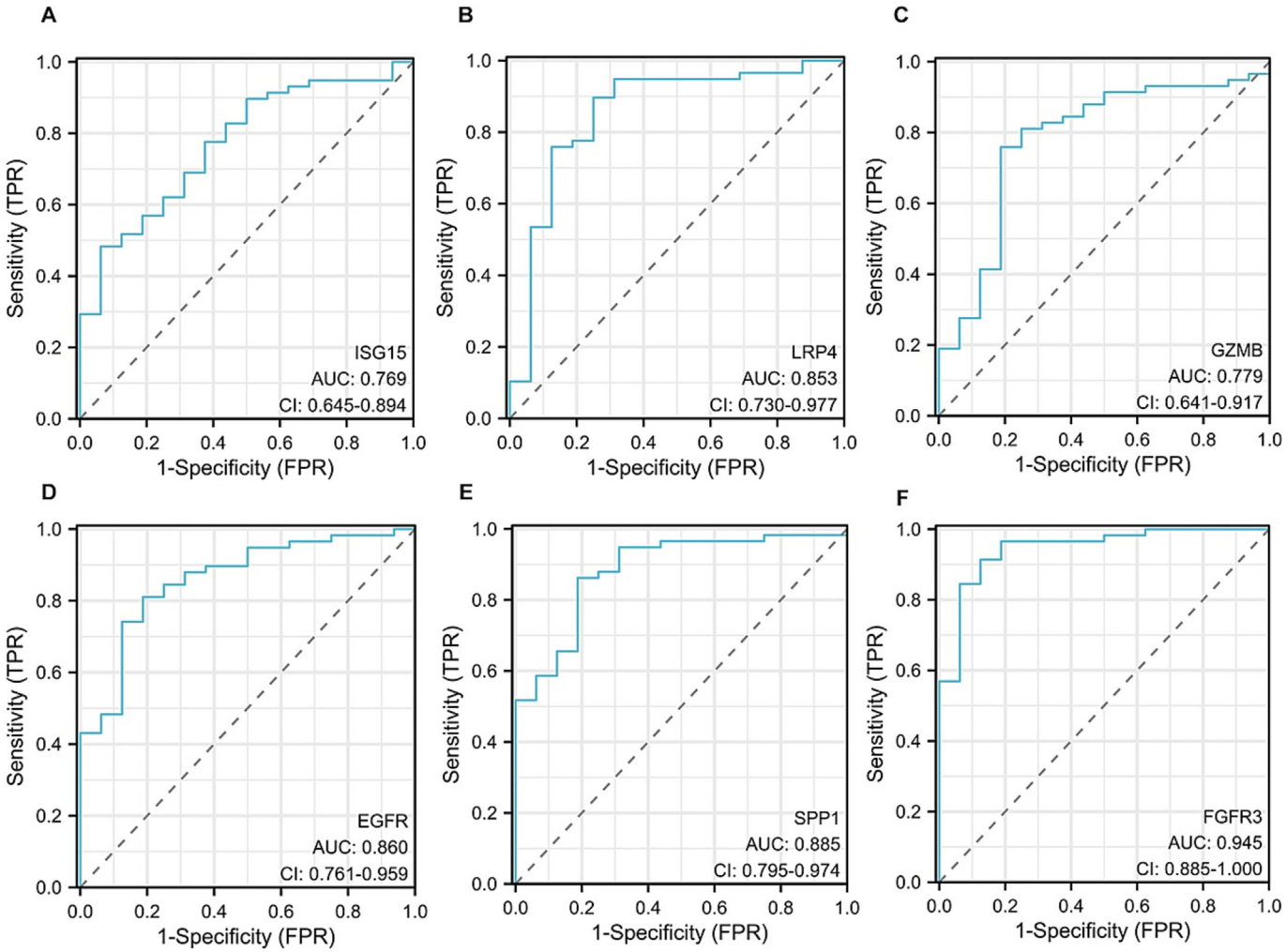

Fig. 8. Differential expression analysis of pyroptosis-related prognostic DEGs in the GSE15605 dataset. **A-F** ROC curves of pyroptosis-related prognostic DEGs *ISG15* (**A**), *LRP4* (**B**), *GZMB* (**C**), EGFR (**D**), SPP1 (**E**), and FGFR3 (**F**) in the GSE15605 dataset. $p > 0.05$, no statistical significance; $p < 0.05$, statistically significant; $p < 0.01$, highly statistically significant; $p < 0.001$, extremely statistically significant. The closer the AUC in the ROC curve was to 1, the better the diagnosis would be. AUC ranged from 0.5 to 0.7 with low accuracy; AUC ranged from 0.7 to 0.9 with some accuracy; High accuracy above 0.9 AUC. *ROC* receiver operating characteristic curve.

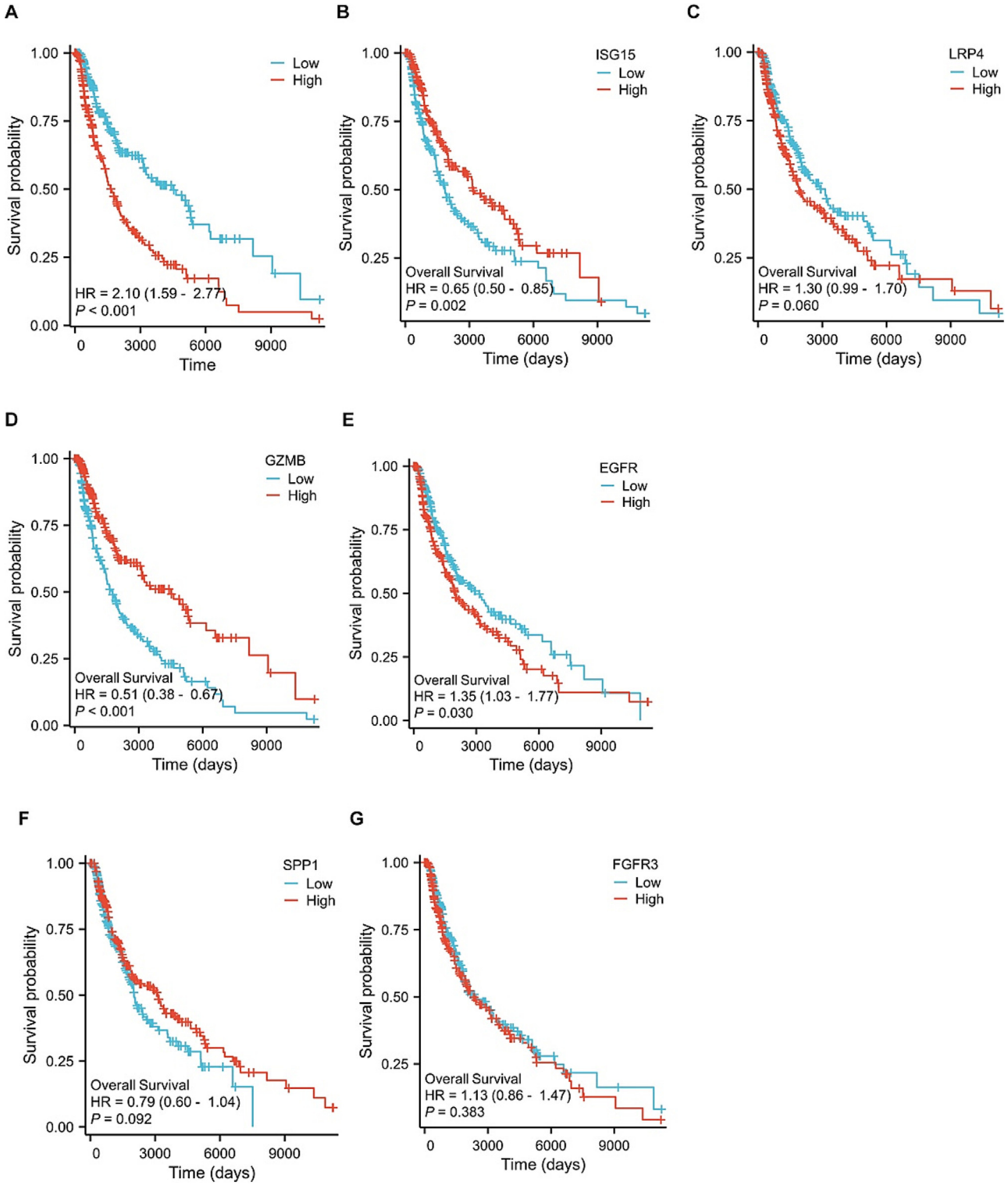

Fig. 9. Prognostic analysis of DEGs related to pyroptosis. **A** KM curve for prognostic analysis of the LASSO regression model of pyroptosis-related prognostic DEGs in the TCGA-SKCM dataset. **B**–**G** Prognostic analysis KM curve of pyroptosis-related prognostic DEGs *ISG15* (**B**), *LRP4* (**C**), *GZMB* (**D**), *EGFR* (**E**), SPP1 (**F**), FGFR3 (**G**) in the TCGA-SKCM data set. $p > 0.05$, no statistical significance; $p < 0.05$, statistically significant; $p < 0.01$, highly statistically significant; $p < 0.001$, extremely statistically significant. *TCGA:* The cancer genome atlas, *SKCM:* cutaneous melanoma, *LASSO:* least absolute shrinkage and selection operator, *KM curve:* Kaplan–Meier curve.

demonstrated that pyroptosis-related prognostic DEGs exhibit heterogeneous genomic alteration patterns in CM. While ISG15 and GZMB showed relatively low mutation frequencies, their prognostic relevance appears to be primarily driven by transcriptional and immune-associated mechanisms rather than genomic instability. In contrast, EGFR displayed frequent and diverse genomic alterations, supporting its multifaceted role in CM progression and its interaction with inflammatory and immune-related pathways.

Table 7
COX regression to identify clinical features of pyroptosis-related differentially expressed genes.

Characteristics	Total (N)	Univariate analysis		Multivariate analysis	
		Hazard ratio (95% CI)	*P*-value	Hazard ratio (95% CI)	*P*-value
Pathologic T stage	362				
T1	42	Reference			
T2	77	1.523 (0.826–2.806)	0.178	1.473 (0.738–2.942)	0.273
T3	90	2.135 (1.179–3.867)	**0.012**	1.884 (0.951–3.731)	0.069
T4	153	3.780 (2.109–6.776)	**<0.001**	3.719 (1.904–7.263)	**<0.001**
Pathologic N stage	403				
N0	225	Reference			
N1	73	1.503 (1.018–2.220)	**0.040**	1.565 (1.017–2.410)	**0.042**
N2	49	1.540 (0.977–2.429)	0.063	1.861 (1.092–3.171)	**0.022**
N3	56	2.744 (1.777–4.236)	**<0.001**	4.052 (2.392–6.862)	**<0.001**
Pathologic M stage	431				
M0	407	Reference			
M1	24	1.902 (1.032–3.506)	0.039	1.495 (0.616–3.628)	0.373
Age	457				
<= 60	247	Reference			
> 60	210	1.663 (1.256–2.201)	**<0.001**	1.293 (0.925–1.807)	0.132
ISG15	457				
Low	230	Reference			
High	227	0.650 (0.495–0.852)	**0.002**	0.925 (0.658–1.300)	0.655
GZMB	457				
Low	228	Reference			
High	229	0.505 (0.383–0.666)	**<0.001**	0.596 (0.419–0.848)	**0.004**
EGFR	457				
Low	226	Reference			
High	231	1.349 (1.030–1.768)	**0.030**	1.455 (1.053–2.011)	**0.023**

3.11. Expression distribution and single-cell profiling of prognostic DEGs associated with pyroptosis

To further characterize the expression patterns of pyroptosis-related prognostic DEGs at the tissue and cellular levels, RNA and protein expression data for ISG15, GZMB, and EGFR were analyzed using the HPA database. Analysis of ISG15 expression revealed elevated RNA levels in tissues enriched with immune activity, including the proximal digestive tract, bone marrow, and lymphoid tissues. Protein-level expression of ISG15 showed limited tissue-specific resolution in HPA, consistent with its inducible nature and context-dependent expression (Fig. 13A). Single-cell analysis of human skin tissue demonstrated that ISG15 expression was primarily associated with immune-related and stromal cell populations, including c-2 T cells, c-5 Langerhans cells, and smooth muscle cell subsets (c-8 and c-11) (Fig. 13B), supporting its involvement in immune and inflammatory processes within the skin microenvironment.

Expression analysis of GZMB showed high RNA and protein levels in bone marrow and lymphoid tissues, consistent with its established role in cytotoxic immune responses. In skin tissue, GZMB protein expression was detectable and predominantly associated with immune cell populations. Single-cell profiling further demonstrated a strong association between GZMB expression and c-2 T cells in human skin (Fig. 13C–D), highlighting its role in immune surveillance and tumor–immune interactions. EGFR exhibited broad RNA expression across multiple tissue types, including skin, connective tissue, liver, gallbladder, endocrine tissues, and female reproductive tissues. Protein expression of EGFR was detected in respiratory tissues, skin, bone marrow, and lymphoid tissues (Fig. 14A). Single-cell analysis of human skin tissue revealed that EGFR expression was most strongly associated with basal keratinocyte populations, particularly c-6 and c-7 basal keratinocytes (Fig. 14B), consistent with its role in epidermal growth and differentiation.

Finally, expression profiling across multiple human tissues and cell lines demonstrated widespread expression of ISG15 across diverse biological systems, including neural, reproductive, skin, and myeloid-derived cell lines (Fig. 14C). In contrast, GZMB showed restricted expression, reflecting its immune cell–specific function (Fig. 14D). Notably, EGFR exhibited high expression in A-431 skin-derived cells (Fig. 14E), consistent with its known overexpression in epithelial malignancies. Collectively, these results demonstrate distinct tissue- and cell-type–specific expression patterns for pyroptosis-related prognostic DEGs. ISG15 and GZMB are predominantly associated with immune-related cell populations, whereas EGFR is primarily expressed in epithelial and keratinocyte populations, supporting their complementary roles in immune regulation, inflammation, and tumor biology in CM.

4. Discussion

Globally, in 2020, SKCM accounted for 57,043 deaths and 324,635 new cases, reflecting its aggressive nature and poor prognosis once advanced [37,38]. Although the post-surgical 5-year survival rate for localized disease approaches 98% [39], this rate declines dramatically to approximately 23% following systemic metastasis [40]. Moreover, a subset of advanced SKCM exhibits resistance to radiotherapy and chemotherapy due to high biological aggressiveness [41]. While immunotherapy and targeted therapy have become central to systemic treatment [42,43], substantial interpatient heterogeneity persists, with individuals at similar clinical stages and undergoing similar treatments demonstrating markedly different outcomes [44,45].

These observations highlight the need for robust molecular biomarkers that can improve prognostic stratification and therapeutic decision-making. Recent advances in sequencing technologies have facilitated the development of multigene prognostic models that reflect pathway-level dysregulation rather than isolated gene effects. Among emerging mechanisms, pyroptosis has gained attention due to its complex role in tumor biology [46,47]. As an inflammatory form of PCD, pyroptosis is closely linked to inflammasome activation and inflammatory signaling, particularly through NLRP3-related pathways [48,49]. Increasing

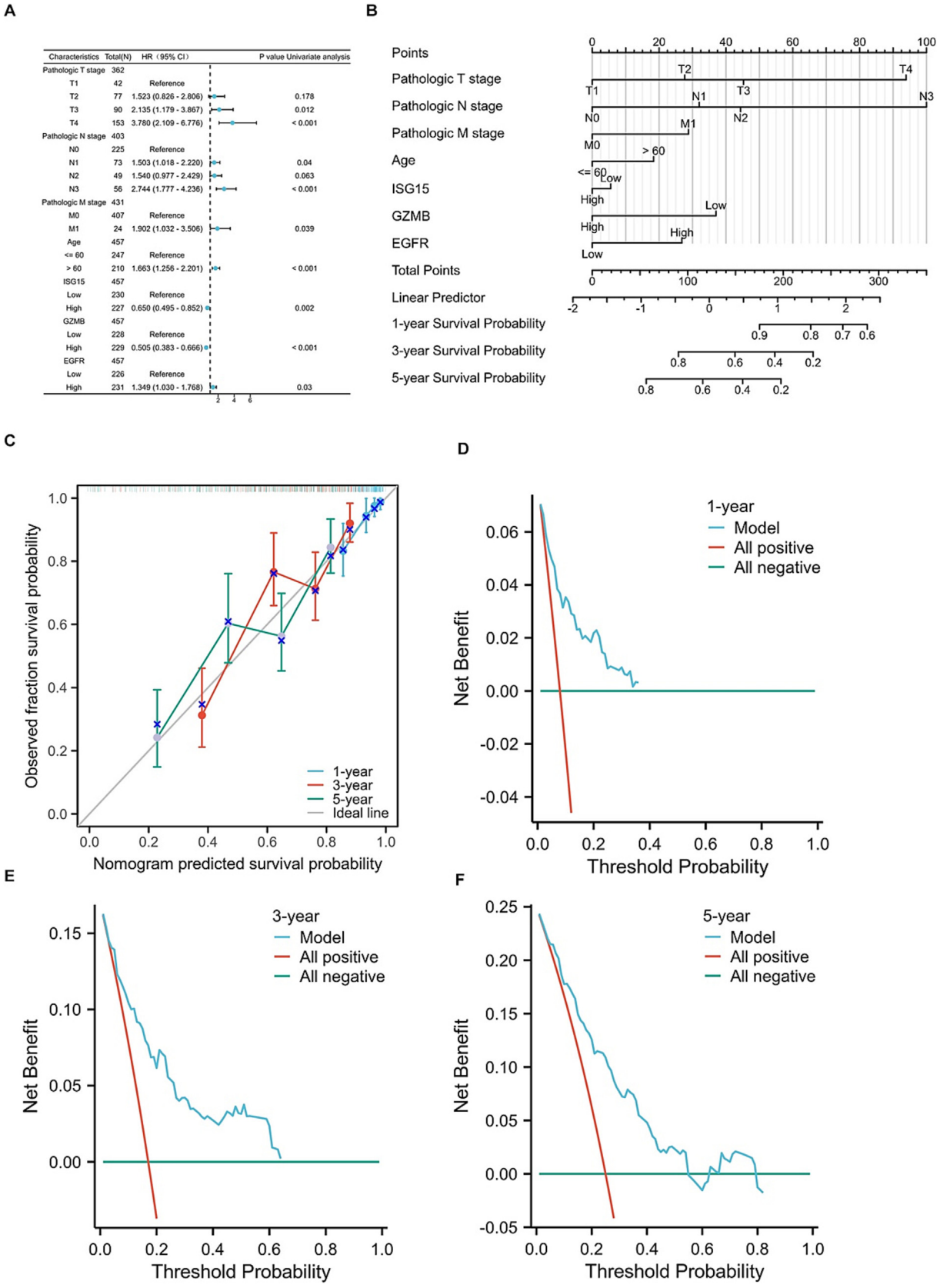

Fig. 10. Prognostic performance of pyroptosis-related prognostic DEGs. **A**–**C** Forest plot (**A**), nomogram (**B**), 1, 3, and 5-year calibration curve plot (**C**) of univariate and multivariate COX regression analysis of pyroptosis-related prognostic DEGs, in the TCGA-SKCM dataset. **D**–**F**: 1-year (**D**), 3-year (**E**), 5-year (**F**) DCA plots of the LASSO-Cox regression prognostic model. *TCGA:* The cancer genome atlas, *SKCM:* cutaneous melanoma, *LASSO:* Least absolute shrinkage and selection operator, *DCA:* decision curve analysis.

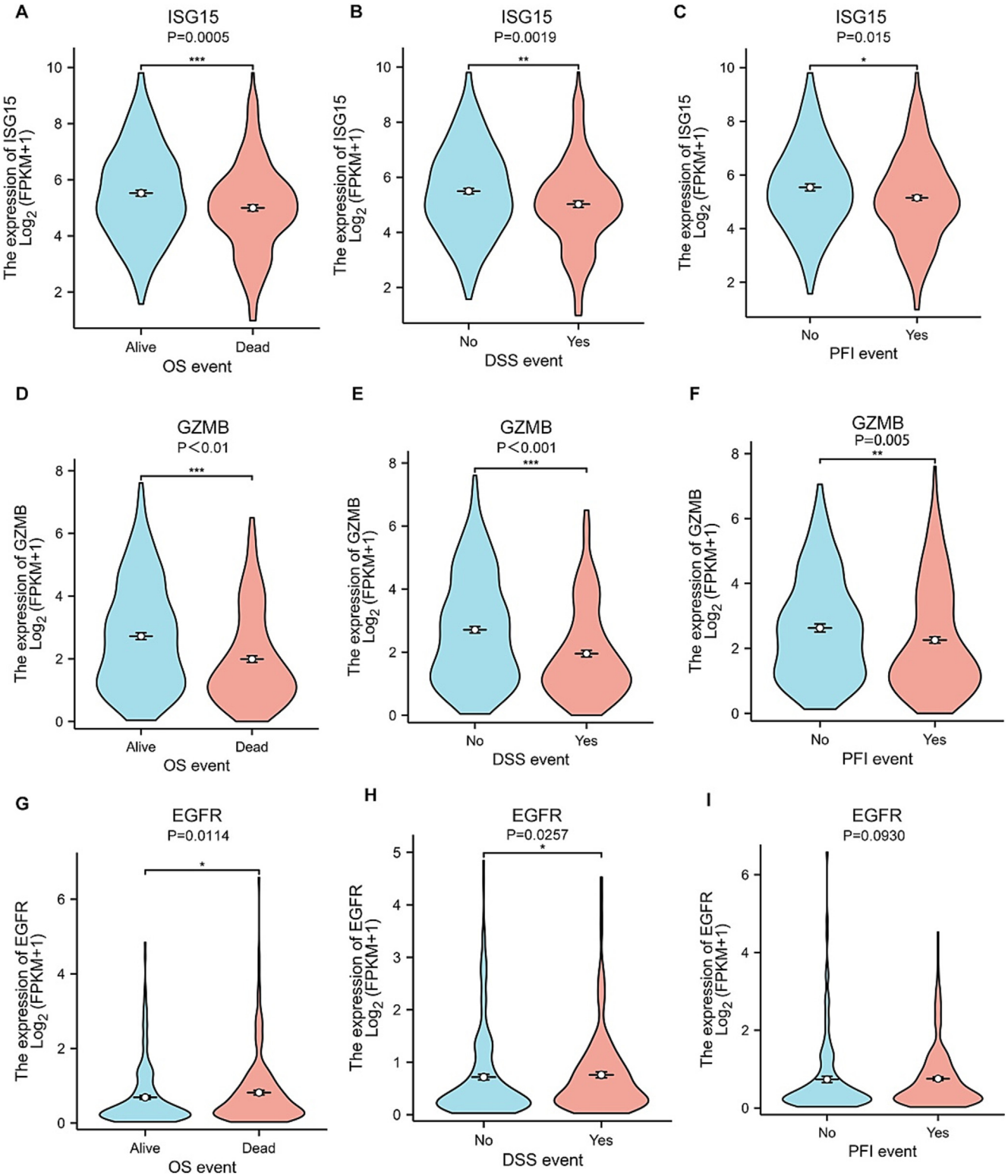

Fig. 11. Clinical analysis of prognostic DEGs related to pyroptosis. **A**–**C** Correlation analysis of pyroptosis-related prognostic differentially expressed gene *CXCL8* with clinical OS (**A**), DSS (**B**), and PFI (**C**) in the TCGA-SKCM dataset. **D**–**F** Correlation analysis of pyroptosis-related prognostic differentially expressed gene GZMB with clinical OS (**D**), DSS (**E**), and PFI (**F**) in the TCGA-SKCM dataset. **G**–**I** Correlation analysis of pyroptosis-related prognostic differentially expressed gene EGFR with clinical OS (**G**), DSS (**H**), and PFI (**I**) in the TCGA-SKCM dataset. $p > 0.05$, no statistical significance; $p < 0.05$, statistically significant; $p < 0.01$, highly statistically significant; $p < 0.001$, extremely statistically significant. *OS* overall survival, *DSS* disease-specific survival, *PFI* progression-free interval.

evidence indicates that pyroptosis profoundly influences immune modulation within the TME [50]. However, pyroptosis can exert both tumor-suppressive and tumor-promoting effects, depending on cellular context and immune interactions [46]. Consequently, its precise contribution to SKCM progression and prognosis remains incompletely understood.

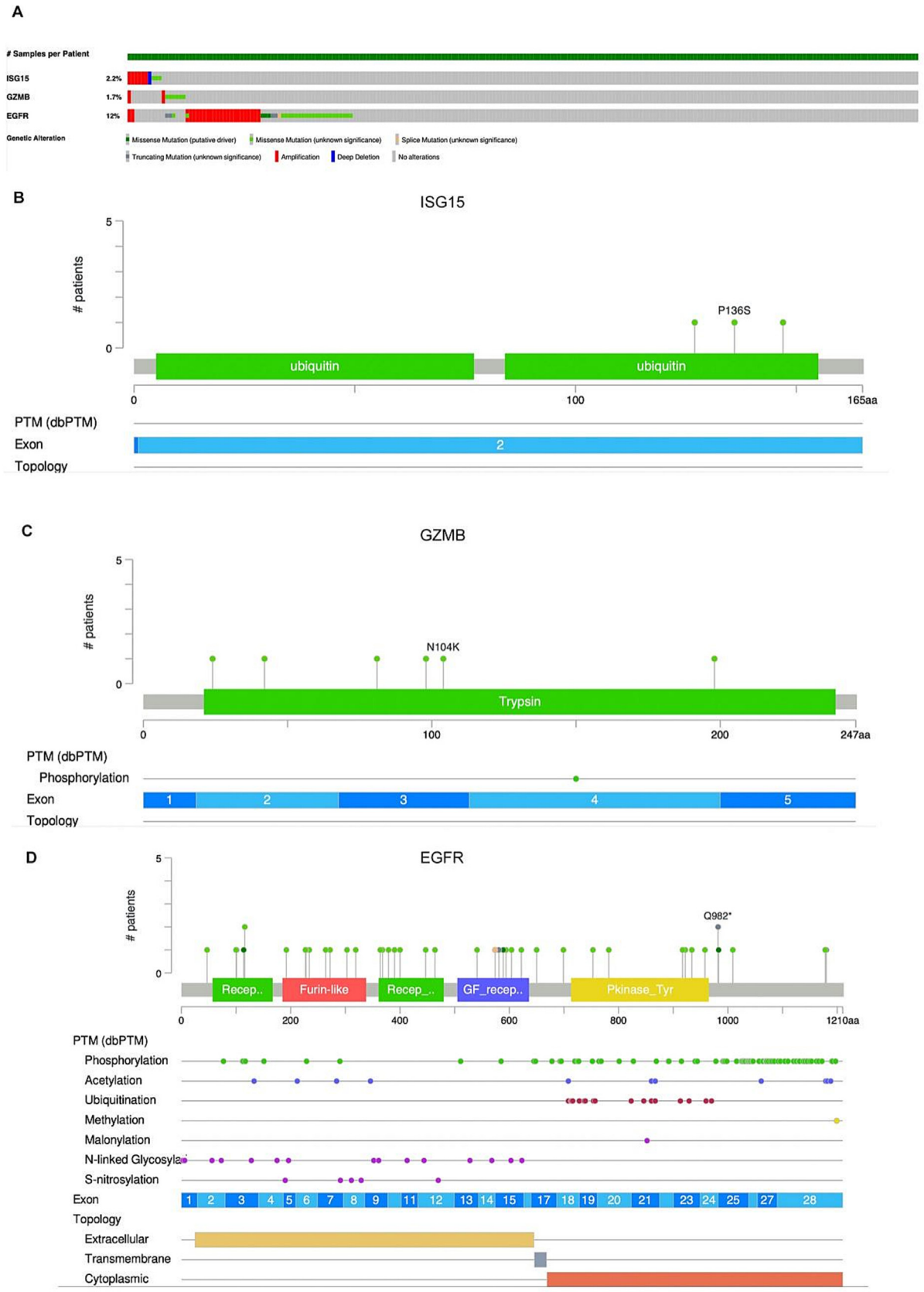

Fig. 12. Mutation analysis of DEGs associated with pyroptosis. **A** Mutation analysis results of pyroptosis-related prognostic DEGs, *ISG15*, *GZMB*, and *EGFR* in the TCGA-SKCM dataset. **B**–**D** Pyroptosis-related prognostic DEGs *ISG15* (**B**), *GZMB*(**C**), *EGFR* (**D**) gene mutation site analysis results in the TCGA-SKCM dataset. All data are from the cBioPortal database. *TCGA:* The cancer genome atlas, *SKCM:* cutaneous melanoma.

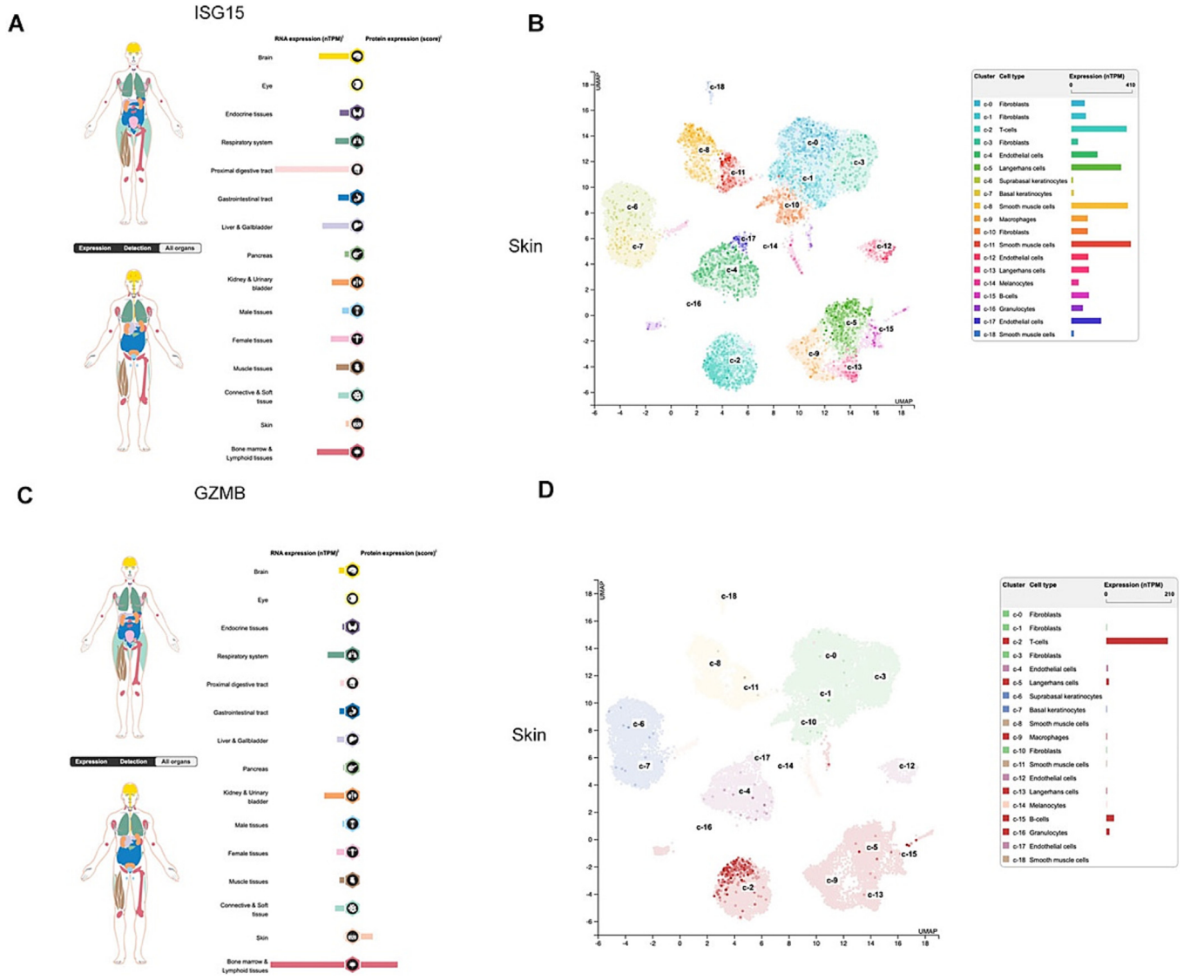

Fig. 13. Analysis of expression distribution of pyroptosis-related prognostic DEGs *ISG15* and *GZMB* and single cell analysis. **A** mRNA and protein expression of *ISG15*, a differentially expressed gene related to pyroptosis, in normal human body tissues. **B** Display of results from single-gene analysis of *ISG15*, a differentially expressed gene related to apoptosis prognosis in the HPA database, in skin tissues. **C** mRNA and protein expression of *GZMB*, a differentially expressed gene related to apoptosis, in normal human body tissues. **D** Single gene analysis of *GZMB*, a differentially expressed gene related to cell scorch in HPA database, in skin tissues. All data are from The Human Protein Atlas database.

In the present study, patient stratification and prognostic prediction were achieved by integrating GEO datasets with TCGA-SKCM data. Eight pyroptosis-related DEGs were consistently identified across datasets, underscoring their robustness. Immune and pathway analyses revealed marked differences in immune-cell composition and biological processes between patient subgroups, suggesting that pyroptosis-related transcriptional alterations contribute to CM heterogeneity. Notably, ISG15 and GZMB emerged as favorable prognostic indicators in both GEO and TCGA cohorts, supporting the concept that specific pyroptosis-related genes can independently predict CM outcomes.

Network-based analyses demonstrated that MMP1 occupied a central position within the PPI and transcriptional regulatory networks. MMP1, a matrix metalloproteinase belonging to the MMP family, plays a key role in ECM degradation and tumor invasion [51,52]. Prior studies have shown that MMP1 promoter polymorphisms are associated with CM susceptibility [53], supporting its functional relevance in melanoma progression. Functional enrichment analyses further indicated that pyroptosis-related DEGs were involved in membrane-associated signaling, UV-response pathways, and receptor tyrosine kinase activity, all of which are biologically relevant to melanoma pathogenesis.

GSEA revealed consistent enrichment of cell cycle–related pathways, including mitotic spindle regulation and chromosomal maintenance, across multiple datasets. These findings align with previous evidence that chromosomal instability is a frequent event in CM and contributes to tumor initiation and progression by impairing DNA replication and spindle checkpoint control [54]. In addition, enrichment of proinflammatory and profibrotic pathways observed in one cohort highlights the inflammatory heterogeneity of CM and supports a link between pyroptosis-related genes and inflammation-driven tumor behavior. This observation is consistent with prior reports demonstrating the diagnostic and prognostic relevance of inflammation-associated markers in CM [55].

Using LASSO regression, six pyroptosis-related DEGs were incorporated into an initial prognostic model, among which ISG15, GZMB, and EGFR retained independent prognostic significance in subsequent survival and Cox regression analyses. Elevated

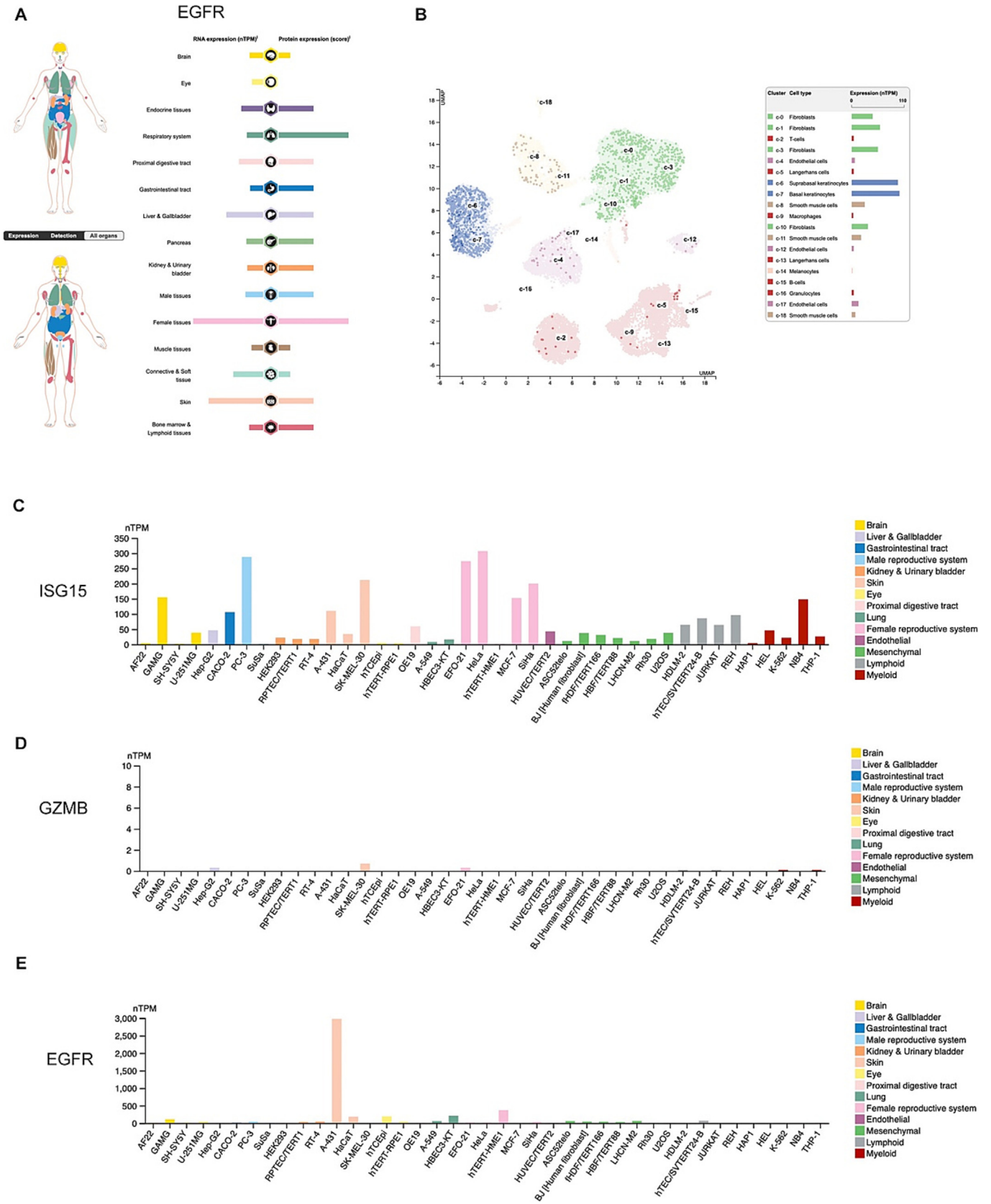

Fig. 14. Analysis of expression distribution of pyroptosis-related prognostic DEGs, *EGFR* and single cell analysis. **A** mRNA and protein expression of *EGFR*, a differentially expressed gene related to pyroptosis, in normal human body tissues. **B** Display of results from single-gene analysis of *EGFR*, a differentially expressed gene related to apoptosis prognosis in the HPA database, in skin tissues. All data are from The Human Protein Atlas database. **C**–**E** Cell line analysis of differentially expressed pyroptosis-related prognostic DEGs genes *ISG15*, *GZMB*, and *EGFR* in homo tissues and organs of the normal human body.

expression of ISG15 and GZMB was associated with improved OS, DSS, and PFI, suggesting that enhanced immune-mediated tumor control contributes to favorable outcomes. ISG15, an interferon-inducible ubiquitin-like modifier, plays a pivotal role in immune regulation and inflammatory signaling [56]. The composition of ISG15 differs among species and tissues. The ISG15 gene produces free ISG15 protein, which is then post-translationally attached to cellular proteins and released into the extracellular environment. ISG15 acts as a modifier, similar to ubiquitin, capable of attaching to substrates in a manner analogous to ubiquitylation, known as ISGylation [57,58,59]. Previous studies have shown that free ISG15 and its conjugates are primarily elevated as a defense mechanism against pathogens in pre-malignant cells and damaged neurons. Nonetheless, the protective mechanism mediated by ISG15/ISGylation becomes deregulated over time, leading to cellular damage and subsequent pathology [60]. Moreover, there is ample evidence indicating that irregular ISG15/ISGylation can lead to the development of tumors, deterioration of neural functions, and inflammation [61,62,63,64,65,66]. GZMB, a prevalent protease, is secreted by NK cells and cytotoxic T lymphocytes and degrades cytokines and ECM proteins. Granzyme B participates in cell death by splitting caspase-3, -7, -9, and -1024. Additionally, granzyme B initiates pyroptosis independently of caspases when introduced into the target cell via the immunological synapse [67,68,69]. The diverse functions of GZMB underscore its vital role in orchestrating immune reactions and cellular protective strategies. Previous studies have suggested that GZMB serves as an indicator of the emergence and evolution of SKCM [70].

Immune infiltration analysis using ssGSEA revealed strong positive correlations between ISG15, GZMB, and immune-cell enrichment, supporting the notion that a favorable prognosis is linked to an immune-active TME. Conversely, LRP4, SPP1, and FGFR3 were negatively correlated with immune infiltration, suggesting potential roles in immune suppression or tumor immune escape. Together, these findings indicate that pyroptosis-related genes influence CM prognosis primarily by modulating tumor–immune interactions rather than through isolated genetic effects.

Several limitations should be acknowledged. The study relied on retrospective public datasets, and sample size limitations may introduce bias. Although multiple independent cohorts were analyzed, prospective validation in larger, well-annotated clinical populations is necessary. Furthermore, the absence of functional experiments limits mechanistic interpretation. Future studies incorporating molecular assays such as PCR, western blotting, immunohistochemistry, and in vivo models are required to validate the biological roles of these genes.

5. Conclusions

In conclusion, by integrating three GEO cohorts with TCGA-SKCM, this study identified eight CM-specific pyroptosis-related DEGs and established reproducible prognostic frameworks for cutaneous melanoma. Among these genes, a robust immune-associated three-gene model comprising ISG15, GZMB, and EGFR demonstrated accurate survival stratification and was closely linked to broad alterations in immune-cell infiltration. These findings suggest that pyroptosis influences CM outcomes primarily through modulation of tumor–immune interactions. Collectively, this work refines risk assessment in CM and highlights pyroptosis-related pathways as biologically and clinically meaningful targets. Future large-scale prospective validation and mechanistic studies are warranted to confirm clinical utility and to further elucidate how pyroptosis-related genes regulate the immune microenvironment in melanoma.

CRediT authorship contribution statement

YaSu Jiang: Writing – original draft, Resources, Investigation, Conceptualization. **YingYing Chen:** Writing – original draft, Resources, Investigation, Conceptualization. **ShengFeng Gao:** Methodology, Data curation. **MengTing Wang:** Methodology, Data curation. **ZhenHua Gong:** Writing – review & editing, Supervision, Project administration, Formal analysis. **JianFeng Ji:** Writing – review & editing, Supervision, Project administration, Formal analysis.

Financial support

The Nantong University Clinical Medicine Special Research Fund Project (No. 2024JY007), The Nantong Science and Technology Bureau (No. MS2023048), the Science Foundation of Kangda College of Nanjing Medical University (KD2025KYJJ194), and the Nantong Municipal Health Commission Scientific Research Project (QNZ2024022).

Supplementary material

https://doi.org/10.1016/j.ejbt.2026.100709.

Data availability

Data will be made available on request.

References

[1] Leonardi GC, Falzone L, Salemi R, et al. Cutaneous melanoma: From pathogenesis to therapy (Review). Int J Oncol 2018;52(4):1071–80. https://doi.org/10.3892/ijo.2018.4287. PMid: 29532857.
[2] Davis LE, Shalin SC, Tackett AJ. Current state of melanoma diagnosis and treatment. Cancer Biol Ther 2019;20(11):1366–79. https://doi.org/10.1080/15384047.2019.1640032. PMid: 31366280.
[3] Hughes MS, Zager J, Faries M, et al. Results of a randomized controlled multicenter phase III trial of percutaneous hepatic perfusion compared with best available care for patients with melanoma liver metastases. Ann Surg Oncol 2016;23(4):1309–19. https://doi.org/10.1245/s10434-015-4968-3. PMid: 26597368.
[4] Zhu Z, Liu W, Gotlieb V. The rapidly evolving therapies for advanced melanoma–Towards immunotherapy, molecular targeted therapy, and beyond. Crit Rev Oncol/Hematol 2016;99:91–9. https://doi.org/10.1016/j.critrevonc.2015.12.002. PMid: 26708040.
[5] Roberts P, Fishman GA, Joshi K, et al. Chorioretinal lesions in a case of melanoma-associated retinopathy treated with pembrolizumab. JAMA Ophthalmol 2016;134(10):1184–8. https://doi.org/10.1001/jamaophthalmol.2016.2944. PMid: 27540851.
[6] Queirolo P, Pfeffer U. Metastatic melanoma: How research can modify the course of a disease. Cancer Metastasis Rev 2017;36(1):3–5. https://doi.org/10.1007/s10555-017-9664-2. PMid: 28197746.
[7] Seftor EA, Seftor REB, Weldon D, et al. Melanoma tumor cell heterogeneity: A molecular approach to study subpopulations expressing the embryonic morphogen nodal. Semin Oncol 2014;41(2):259–66. https://doi.org/10.1053/j.seminoncol.2014.02.001. PMid: 24787297.
[8] Shannan B, Perego M, Somasundaram R. Heterogeneity in melanoma. In: Kaufman H, Mehnert J, editors. Melanoma. Cancer treatment and research. Cham: Springer; 2016. p. 1–15. https://doi.org/10.1007/978-3-319-22539-5_1. PMid: 26601857.
[9] Zhang Q, Liu W, Zhang HM, et al. hTFtarget: A comprehensive database for regulations of human transcription factors and their targets. Genom Proteom Bioinform 2020;18(2):120–8. https://doi.org/10.1016/j.gpb.2019.09.006. PMid: 32858223.
[10] Xue Y, Li J, Lu X. A novel immune-related prognostic signature for thyroid carcinoma. Technol Cancer Res Treat 2020;19:1533033820935860. https://doi.org/10.1177/1533033820935860. PMid: 32588760.
[11] Bao M, Zhang L, Hu Y. Novel gene signatures for prognosis prediction in ovarian cancer. J Cell Mol Med 2020;24(17):9972–84. https://doi.org/10.1111/jcmm.15601. PMid: 32666642.
[12] Wei Y, Yang L, Pandeya A, et al. Pyroptosis-induced inflammation and tissue damage. J Mol Biol 2022;434(4):167301. https://doi.org/10.1016/j.jmb.2021.167301. PMid: 34653436.

[13] Lu L, Zhang Y, Tan X, et al. Emerging mechanisms of pyroptosis and its therapeutic strategy in cancer. Cell Death Discov 2022;8(1):338. https://doi.org/10.1038/s41420-022-01101-6. PMid: 35896522.
[14] Cao Y, Xie J, Chen L, et al. Construction and validation of a novel pyroptosis-related gene signature to predict the prognosis of uveal melanoma. Front Cell Dev Biol 2021;9:761350. https://doi.org/10.3389/fcell.2021.761350. PMid: 34901006.
[15] Zhuang Z, Cai H, Lin H, et al. Development and validation of a robust pyroptosis-related signature for predicting prognosis and immune status in patients with colon cancer. J Oncol 2021;2021:5818512. https://doi.org/10.1155/2021/5818512. PMid: 34840571.
[16] Colaprico A, Silva TC, Olsen C, et al. TCGAbiolinks: An R/Bioconductor package for integrative analysis of TCGA data. Nucl Acids Res 2016;44(8):e71. https://doi.org/10.1093/nar/gkv1507. PMid: 26704973.
[17] Goldman MJ, Craft B, Hastie M, et al. Visualizing and interpreting cancer genomics data via the Xena platform. Nat Biotechnol 2020;38(6):675–8. https://doi.org/10.1038/s41587-020-0546-8. PMid: 32444850.
[18] Ritchie ME, Phipson B, Wu D, et al. *limma* powers differential expression analyses for RNA-sequencing and microarray studies. Nucl Acids Res 2015;43(7):e47. https://doi.org/10.1093/nar/gkv007. PMid: 25605792.
[19] Stelzer G, Rosen N, Plaschkes I, et al. The GeneCards Suite: From gene data mining to disease genome sequence analyses. Curr Protoc Bioinform 2016;54:1.30.1–1.30.33. https://doi.org/10.1002/cpbi.5. PMid: 27322403.
[20] Liberzon A, Birger C, Thorvaldsdóttir H, et al. The molecular signatures database hallmark gene set collection. Cell Syst 2015;1(6):417–25. https://doi.org/10.1016/j.cels.2015.12.004. PMid: 26771021.
[21] Yu G. Gene ontology semantic similarity analysis using GOSemSim. In: Kidder B, editor. Stem Cell Transcriptional Networks. Methods in Molecular Biology. New York, NY: Humana; 2020. p. 207–15. https://doi.org/10.1007/978-1-0716-0301-7_11. PMid: 31960380.
[22] Yu G, Wang LG, Han Y, et al. clusterProfiler: An R package for comparing biological themes among gene clusters. OMICS J Integr Biol 2012;16(5):284–7. https://doi.org/10.1089/omi.2011.0118. PMid: 22455463.
[23] Subramanian A, Tamayo P, Mootha VK, et al. Gene set enrichment analysis: A knowledge-based approach for interpreting genome-wide expression profiles. Proc Natl Acad Sci USA 2005;102(43):15545. https://doi.org/10.1073/pnas.0506580102. PMid: 16199517.
[24] Hänzelmann S, Castelo R, Guinney J. GSVA: Gene set variation analysis for microarray and RNA-seq data. BMC Bioinf 2013;14:7. https://doi.org/10.1186/1471-2105-14-7. PMid: 23323831.
[25] Charoentong P, Finotello F, Angelova M, et al. Pan-cancer immunogenomic analyses reveal genotype-immunophenotype relationships and predictors of response to checkpoint blockade. Cell Rep 2017;18(1):248–62. https://doi.org/10.1016/j.celrep.2016.12.019. PMid: 28052254.
[26] Barbie DA, Tamayo P, Boehm JS, et al. Systematic RNA interference reveals that oncogenic *KRAS*-driven cancers require TBK1. Nature 2009;462(7269):108–12. https://doi.org/10.1038/nature08460. PMid: 19847166.
[27] Szklarczyk D, Gable AL, Lyon D, et al. STRING v11: Protein-protein association networks with increased coverage, supporting functional discovery in genome-wide experimental datasets. Nucl Acids Res 2019;47(D1):D607–13. https://doi.org/10.1093/nar/gky1131. PMid: 30476243.
[28] Li JH, Liu S, Zhou H, et al. starBase v2.0: Decoding miRNA-ceRNA, miRNA-ncRNA and protein-RNA interaction networks from large-scale CLIP-Seq data. Nucl Acids Res 2014;42(D1):D92–7. https://doi.org/10.1093/nar/gkt1248. PMid: 24297251.
[29] Chen Y, Wang X. miRDB: An online database for prediction of functional microRNA targets. Nuclic Acids Res 2020;48(D1):D127–31. https://doi.org/10.1093/nar/gkz757. PMid: 31504780.
[30] Yang JH, Li JH, Jiang S, et al. ChIPBase: A database for decoding the transcriptional regulation of long non-coding RNA and microRNA genes from ChIP-Seq data. Nucleic Acids Res 2013;41(D1):D177–87. https://doi.org/10.1093/nar/gks1060. PMid: 23161675.
[31] Freshour SL, Kiwala S, Cotto KC, et al. Integration of the Drug-Gene Interaction Database (DGIdb 4.0) with open crowdsource efforts. Nucleic Acids Res 2021;49(D1):D1144–51. https://doi.org/10.1093/nar/gkaa1084. PMid: 33237278.
[32] Mandrekar JN. Receiver operating characteristic curve in diagnostic test assessment. J Thorac Oncol 2010;5(9):1315–6. https://doi.org/10.1097/JTO.0b013e3181ec173d. PMid: 20736804.
[33] Hajian-Tilaki K. Receiver Operating Characteristic (ROC) curve analysis for medical diagnostic test evaluation. Caspian J Internal Med 2013;4(2):627–35. PMid: 24009950.
[34] Tataranni T, Piccoli C. Dichloroacetate (DCA) and cancer: An overview towards clinical applications. Oxid Med Cell Longev 2019;2019:8201079. https://doi.org/10.1155/2019/8201079. PMid: 31827705.
[35] Thul PJ, Lindskog C. The human protein atlas: A spatial map of the human proteome. Protein Sci 2018;27(1):233–44. https://doi.org/10.1002/pro.3307. PMid: 28940711.
[36] Hanley JA, McNeil BJ. The meaning and use of the area under a receiver operating characteristic (ROC) curve. Radiology 1982;143(1):29–36. https://doi.org/10.1148/radiology.143.1.7063747. PMid: 7063747.
[37] Wang H, Xie X, Zhu J, et al. Comprehensive analysis identifies IFI16 as a novel signature associated with overall survival and immune infiltration of skin cutaneous melanoma. Cancer Cell Int 2021;21(1):694. https://doi.org/10.1186/s12935-021-02409-6. PMid: 34930258.
[38] Sung H, Ferlay J, Siegel RL, et al. Global Cancer Statistics 2020: GLOBOCAN estimates of incidence and mortality worldwide for 36 cancers in 185 countries. CA Cancer J Clin 2021;71(3):209–49. https://doi.org/10.3322/caac.21660. PMid: 33538338.
[39] Swetter SM, Tsao H, Bichakjian CK, et al. Guidelines of care for the management of primary cutaneous melanoma. J Am Acad Dermatol 2019;80(1):208–50. https://doi.org/10.1016/j.jaad.2018.08.055. PMid: 30392755.
[40] Rebecca VW, Somasundaram R, Herlyn M. Pre-clinical modeling of cutaneous melanoma. Nat Commun 2020;11(1):2858. https://doi.org/10.1038/s41467-020-15546-9. PMid: 32504051.
[41] Ping S, Wang S, Zhao Y, et al. Identification and validation of a ferroptosis-related gene signature for predicting survival in skin cutaneous melanoma. Cancer Med 2022;11(18):3529–41. https://doi.org/10.1002/cam4.4706. PMid: 35373463.
[42] Ribas A, Lawrence D, Atkinson V, et al. Combined BRAF and MEK inhibition with PD-1 blockade immunotherapy in *BRAF*-mutant melanoma. Nat Med 2019;25(6):936–40. https://doi.org/10.1038/s41591-019-0476-5. PMid: 31171879.
[43] Pelster MS, Amaria RN. Combined targeted therapy and immunotherapy in melanoma: A review of the impact on the tumor microenvironment and outcomes of early clinical trials. Ther Adv Med Oncol 2019;11:1758835919830826. https://doi.org/10.1177/1758835919830826. PMid: 30815041.
[44] Simeone E, Grimaldi AM, Festino L, et al. Correlation between previous treatment with BRAF inhibitors and clinical response to pembrolizumab in patients with advanced melanoma. OncoImmunology 2017;6(3):e1283462. https://doi.org/10.1080/2162402X.2017.1283462. PMid: 28405510.
[45] Hassel JC, Lee SB, Meiss F, et al. Vemurafenib and ipilimumab: A promising combination? Results of a case series. OncoImmunology 2016;5(4):e1101207. https://doi.org/10.1080/2162402X.2015.1101207. PMid: 27141385.
[46] Xia X, Wang X, Cheng Z, et al. The role of pyroptosis in cancer: Pro-cancer or pro-"host"? Cell Death Dis 2019;10(9):650. https://doi.org/10.1038/s41419-019-1883-8. PMid: 31501419.
[47] Hsu SK, Li CY, Lin IL, et al. Inflammation-related pyroptosis, a novel programmed cell death pathway, and its crosstalk with immune therapy in cancer treatment. Theranostics 2021;11(18):8813–35. https://doi.org/10.7150/thno.62521. PMid: 34522213.
[48] Yang Y, Liu PY, Bao W, et al. Hydrogen inhibits endometrial cancer growth via a ROS/NLRP3/caspase-1/GSDMD-mediated pyroptotic pathway. BMC Cancer 2020;20:28. https://doi.org/10.1186/s12885-019-6491-6. PMid: 31924176.
[49] Zhang J, Jiang N, Zhang L, et al. NLRP6 expressed in astrocytes aggravates neurons injury after OGD/R through activating the inflammasome and inducing pyroptosis. Int Immunopharmacol 2020;80:106183. https://doi.org/10.1016/j.intimp.2019.106183. PMid: 31927506.
[50] He X, Fan X, Bai B, et al. Pyroptosis is a critical immune-inflammatory response involved in atherosclerosis. Pharmacol Res 2021;165:105447. https://doi.org/10.1016/j.phrs.2021.105447. PMid: 33516832.
[51] Berwick M, Lachiewicz A, Pestak C. Solar UV exposure and mortality from skin tumors. In: Reichrath J, editor. Sunlight, vitamin D and skin cancer. advances in experimental medicine and biology. New York, NY: 124Springer; 2008. p. 117. https://doi.org/10.1007/978-0-387-77574-6_10. PMid: 18348452.
[52] Fargnoli MC, Argenziano G, Zalaudek I, et al. High- and low-penetrance cutaneous melanoma susceptibility genes. Expert Rev Anticancer Ther 2006;6(5):657–70. https://doi.org/10.1586/14737140.6.5.657. PMid: 16759158.
[53] Wang LE, Huang YJ, Yin M, et al. Promoter polymorphisms in *Matrix metallopeptidase* 1 and risk of cutaneous melanoma. Eur J Cancer 2011;47(1):107–15. https://doi.org/10.1016/j.ejca.2010.06.129. PMid: 20655738.
[54] Liu N, Liu G, Ma Q, et al. Chromosome instability-associated prognostic signature and cluster investigation for cutaneous melanoma cases. IET Syst Biol 2023;17(3):121–30. https://doi.org/10.1049/syb2.12064. PMid: 37186446.
[55] Ene CD, Tampa M, Nicolae I, et al. Antiganglioside antibodies and inflammatory response in cutaneous melanoma. J Immunol Res 2020;2020:2491265. https://doi.org/10.1155/2020/2491265. PMid: 32855975.
[56] Desai SD, Haas AL, Wood LM, et al. Elevated expression of ISG15 in tumor cells interferes with the ubiquitin/26S proteasome pathway. Cancer Res 2006;66(2):921–8. https://doi.org/10.1158/0008-5472.CAN-05-1123. PMid: 16424026.
[57] Loeb KR, Haas AL. The interferon-inducible 15-kDa ubiquitin homolog conjugates to intracellular proteins. J Biol Chem 1992;267(11):7806–13. https://doi.org/10.1016/S0021-9258(18)42585-9. PMid: 1373138.
[58] Tong HV, Hoan NX, Binh MT, et al. Upregulation of enzymes involved in ISGylation and Ubiquitination in patients with hepatocellular carcinoma. Int J Med Sci 2020;17(3):347–53. https://doi.org/10.7150/ijms.39823. PMid: 32132870.
[59] Narasimhan J, Potter JL, Haas AL. Conjugation of the 15-kDa interferon-induced ubiquitin homolog is distinct from that of ubiquitin. J Biol Chem 1996;271(1):324–30. https://doi.org/10.1074/jbc.271.1.324. PMid: 8550581.
[60] Paladino P, Cummings DT, Noyce RS, et al. The IFN-independent response to virus particle entry provides a first line of antiviral defense that is independent of TLRs and retinoic acid-inducible gene I. J Immunol 2006;177(11):8008–16. https://doi.org/10.4049/jimmunol.177.11.8008. PMid: 17114474.
[61] Desai SD. ISG15: A double edged sword in cancer. OncoImmunology 2015;4(12):e1052935. https://doi.org/10.1080/2162402X.2015.1052935. PMid: 26587329.

[62] Buda G, Valdez RM, Biagioli G, et al. Inflammatory cutaneous lesions and pulmonary manifestations in a new patient with autosomal recessive ISG15 deficiency case report. Allergy Asthma Clin Immunol 2020;16:77. https://doi.org/10.1186/s13223-020-00473-7. PMid: 32944031.
[63] Malik MNH, Waqas SF, Zeitvogel J, et al. Congenital deficiency reveals critical role of ISG15 in skin homeostasis. J Clin Invest 2022;132(3):e141573. https://doi.org/10.1172/JCI141573. PMid: 34847081.
[64] Martin-Fernandez M, Bravo García-Morato M, Gruber C, et al. Systemic type I IFN inflammation in human ISG15 deficiency leads to necrotizing skin lesions. Cell Rep 2020;31(6):107633. https://doi.org/10.1016/j.celrep.2020.107633. PMid: 32402279.
[65] Cao X. ISG15 secretion exacerbates inflammation in SARS-CoV-2 infection. Nat Immunol 2021;22(11):1360–2. https://doi.org/10.1038/s41590-021-01056-3. PMid: 34671145.
[66] Liu G, Lee JH, Parker ZM, et al. ISG15-dependent activation of the sensor MDA5 is antagonized by the SARS-CoV-2 papain-like protease to evade host innate immunity. Nat Microbiol 2021;6(4):467–78. https://doi.org/10.1038/s41564-021-00884-1. PMid: 33727702.
[67] Hameed A, Lowrey DM, Lichtenheld M, et al. Characterization of three serine esterases isolated from human IL-2 activated killer cells. J Immunol 1988;141(9):3142–7. https://doi.org/10.4049/jimmunol.141.9.3142. PMid: 3262682.
[68] Krähenbühl O, Rey C, Jenne D, et al. Characterization of granzymes A and B isolated from granules of cloned human cytotoxic T lymphocytes. J Immunol 1988;141(10):3471–7. PMid: 3263427.
[69] Poe M, Blake JT, Boulton DA, et al. Human cytotoxic lymphocyte granzyme B. Its purification from granules and the characterization of substrate and inhibitor specificity. J Biol Chem 1991;266(1):98–103. https://doi.org/10.1016/S0021-9258(18)52407-8.
[70] Liang Z, Pan L, Shi J, Zhang L. *C1QA*, *C1QB*, and *GZMB* are novel prognostic biomarkers of skin cutaneous melanoma relating tumor microenvironment. Sci Rep 2022;12(1):20460. https://doi.org/10.1038/s41598-022-24353-9. PMid: 36443341.